

Mesoscale Molecular Simulations of Fabry–Pérot Vibrational Strong Coupling

Tao E. Li^{a)}

Department of Physics and Astronomy, University of Delaware, Newark, Delaware 19716, USA

Developing theoretical frameworks for vibrational strong coupling (VSC) beyond the single-mode approximation is crucial for a comprehensive understanding of experiments with planar Fabry–Pérot cavities. Herein, a generalized cavity molecular dynamics (CavMD) scheme is developed to simulate VSC of a large ensemble of realistic molecules coupled to an arbitrary 1D or 2D photonic environment. This approach is built upon the Power–Zienau–Woolley Hamiltonian in the normal mode basis and uses a grid representation of the molecular ensembles to reduce the computational cost. When simulating the polariton dispersion relation for a homogeneous distribution of molecules in planar Fabry–Pérot cavities, our data highlight the importance of preserving the in-plane translational symmetry of the molecular distribution. In this homogeneous limit, CavMD yields the consistent polariton dispersion relation as an analytic theory, i.e., incorporating many cavity modes with varying in-plane wave vectors (k_{\parallel}) produces the same spectrum as the system with a single cavity mode. Furthermore, CavMD reveals that the validity of the single mode approximation is challenged when nonequilibrium polariton dynamics are considered, as polariton-polariton scattering occurs between modes with nearest neighbor k_{\parallel} . The procedure for numerically approaching the macroscopic limit is also demonstrated with CavMD by increasing the system size. Looking forward, our generalized CavMD approach may facilitate understanding vibrational polariton transport and condensation.

I. INTRODUCTION

Vibrational strong coupling (VSC) has recently attracted great attention due to its potential for modifying molecular properties with vacuum electromagnetic fields.^{1–9} Most VSC experiments to date have been performed in planar Fabry–Pérot cavities, in which the Rabi splitting between an infrared (IR) cavity mode and a vibrational mode of a large collection of molecules is observed in the linear IR spectrum.^{10–15} Alongside the exciting yet sometimes controversial experimental observations,^{16–18} theoretical work on VSC^{19–35} usually builds upon different levels of approximations; the most pervasive approximation being that only a single or a few cavity modes are taken into account. However, as will be discussed in detail in this work, because planar Fabry–Pérot cavities contain a continuum of cavity modes along the cavity mirror plane,¹¹ the single-mode approximation might break down.

For example, under electronic strong coupling, experimentally observed exciton-polariton condensates originate from elastic scattering between lower polaritons at different in-plane wave vectors (as denoted by k_{\parallel}).^{36,37} In other words, including cavity modes at different k_{\parallel} values is necessary for a proper description of exciton-polariton condensates. As another example, Ebbesen and coworkers observed that VSC catalytic effects occur only when the cavity mode at $k_{\parallel} = 0$ is at resonance with a vibrational mode of molecules.^{3,5} These examples make it clear that the single-mode approximation is insufficient for describing these strong coupling effects in Fabry–Pérot cav-

ities, and the full cavity dispersion relation must be considered.

Some recent studies have employed numerical simulations to investigate electronic strong coupling in multi-mode one-dimensional (1D) Fabry–Pérot cavities.^{38–41} Under VSC conditions, however, most theoretical approaches have relied on the single-mode approximation, with an explicit treatment of the multi-mode Fabry–Pérot cavities discussed only for model systems.^{42,43} It is thus necessary to extend theoretical approaches for VSC, including electronic structure theory and molecular dynamics simulations, to the multi-mode case. Moreover, only by developing an adequate theoretical description of the multi-mode cavities, one can examine whether conclusions made in the single-mode limit still hold for more realistic cavity setups.

One efficient simulation tool for describing VSC in the single-mode limit is the cavity molecular dynamics (CavMD) approach,³³ in which the dynamics of a large ensemble of molecules coupled to a single cavity mode (or a few cavity modes) are propagated classically or semi-classically (via path integrals) on the electronic ground state surface. Some notable results of CavMD when simulating collective VSC are worth mentioning. (i) Under thermal equilibrium, cavity modifications of individual molecular properties become negligible even when nuclear and photonic quantum effects are considered.^{33,44} (ii) In the linear response limit, the polariton spectrum described by CavMD is equivalent to that described by coupled oscillator models.^{33,45} (iii) In the weak excitation limit, the relaxation rates of the upper polariton (UP) have the same parameter dependence as the Fermi’s golden rule rate of a tight-binding harmonic model.⁴⁶ (iv) In strong pumping regime, CavMD predicts novel mechanisms, including lower-polariton (LP) enhanced molec-

^{a)}Electronic mail: taoli@udel.edu

ular nonlinear absorption,⁴⁷ a behavior that has been observed experimentally,⁴⁸ as well as strong energy accumulation in solute molecules by exciting the solvent LP.⁴⁹ The CavMD approach has also recently embraced a quantum mechanical/molecular mechanical (QM/MM) description of the molecular systems. This advance enables the direct simulation of ultrafast VSC experiments such as the pseudorotation “reaction” of the Fe(CO)₅ solute in the *n*-dodecane solvent,⁵⁰ although more extensive simulations (i.e., by including a large number of replicas of the solute-solvent molecular systems) are needed to understand the mechanisms of the ultrafast experiments.

In this manuscript, we extend the CavMD approach to describe VSC in arbitrary cavity setups, especially Fabry–Pérot cavities with k_{\parallel} -dependent cavity modes. We perform numerical experiments to highlight the importance of the in-plane translational symmetry in reproducing the k_{\parallel} -dependent polariton branches observed in experiments. Additionally, utilizing nonequilibrium CavMD simulations, we provide initial data on polariton-polariton scattering with neighboring k_{\parallel} values, a fundamental mechanism which is relevant to the formation of polariton condensates. Finally, our numerical experiments suggest research opportunities of preparing VSC in the absence of the molecular in-plane translational symmetry.

The manuscript is organized as follows. In Sec. II, we present a derivation of CavMD in arbitrary photonic environments, especially in Fabry–Pérot-like cavities. Sec. III provides simulation details. In Sec. IV, we present CavMD results for a few cavity setups. In Sec. V, we discuss the importance of the in-plane translational symmetry and the procedure to approach the macroscopic limit using CavMD. We conclude in Sec. VI.

II. THEORY

A. QED Hamiltonian in a photonic structure

We start with the Power–Zienau–Woolley Hamiltonian for light-matter interactions:⁵¹

$$\hat{H}_{\text{QED}} = \hat{H}_{\text{M}} + \hat{H}_{\text{ph}} + \hat{H}_{\text{int}}. \quad (1)$$

Here, \hat{H}_{M} denotes the standard molecular (kinetic + potential) Hamiltonian; \hat{H}_{ph} denotes the photonic Hamiltonian:

$$\hat{H}_{\text{ph}} = \frac{1}{2} \int d\mathbf{r} \left(\frac{1}{\varepsilon_0} |\hat{\mathbf{D}}_{\perp}(\mathbf{r})|^2 + \frac{1}{\mu_0} |\hat{\mathbf{B}}(\mathbf{r})|^2 \right), \quad (2)$$

where $\hat{\mathbf{D}}_{\perp}(\mathbf{r})$ and $\hat{\mathbf{B}}(\mathbf{r})$ are the displacement and magnetic field operators, and ε_0 and μ_0 denote the vacuum permittivity and permeability, respectively; \hat{H}_{int} denotes the Hamiltonian that governs the light-matter interaction:

$$\hat{H}_{\text{int}} = -\frac{1}{\varepsilon_0} \int d\mathbf{r} \hat{\mathbf{D}}_{\perp}(\mathbf{r}) \cdot \hat{\mathcal{P}}_{\perp}(\mathbf{r}) + \frac{1}{2\varepsilon_0} \int d\mathbf{r} |\hat{\mathcal{P}}_{\perp}(\mathbf{r})|^2. \quad (3)$$

Here, the transverse polarization density operator $\hat{\mathcal{P}}_{\perp}(\mathbf{r})$ is defined as⁵¹

$$\hat{\mathcal{P}}_{\perp}(\mathbf{r}) = \int d\mathbf{r}' \overleftrightarrow{\delta}_{\perp}(\mathbf{r} - \mathbf{r}') \hat{\mathcal{P}}(\mathbf{r}'), \quad (4)$$

where the polarization density operator $\hat{\mathcal{P}}(\mathbf{r})$ reads

$$\hat{\mathcal{P}}(\mathbf{r}) = \sum_i Q_i \hat{\mathbf{r}}_i \delta(\mathbf{r} - \mathbf{r}_i). \quad (5)$$

In Eq. (5), Q_i denotes the charge of the i -th particle, which can be either an electron or a nucleus; $\hat{\mathbf{r}}_i$ denotes the position operator of the particle. In Eq. (4), the transverse δ -function $\overleftrightarrow{\delta}_{\perp}(\mathbf{r} - \mathbf{r}')$ is a rank-two tensor:

$$\overleftrightarrow{\delta}_{\perp}(\mathbf{r} - \mathbf{r}') = \sum_{k\lambda} \mathbf{f}_{k\lambda}(\mathbf{r}) \mathbf{f}_{k\lambda}^*(\mathbf{r}'). \quad (6)$$

Here, $\mathbf{f}_{k\lambda}(\mathbf{r})$ denotes the mode function of the photon with wave vector $k \equiv |\mathbf{k}|$ and two possible polarization directions indexed by λ , and $\mathbf{f}_{k\lambda}^*(\mathbf{r})$ denotes its complex conjugate. The explicit form of $\mathbf{f}_{k\lambda}(\mathbf{r})$ depends on the boundary conditions of the dielectric medium; it can be obtained by solving the Helmholtz equation $\nabla \times \nabla \times \mathbf{f}_{k\lambda} - k^2 \mathbf{f}_{k\lambda} = 0$. For example, in vacuum, $\mathbf{f}_{k\lambda}(\mathbf{r}) = \boldsymbol{\xi}_{\lambda} e^{i\mathbf{k} \cdot \mathbf{r}} / \sqrt{\Omega}$, where $\boldsymbol{\xi}_{\lambda}$ denotes the unit vector along the photon polarization direction, and Ω denotes the quantization volume.

1. Normal mode representation

The field operators in Eqs. (2) and (3) can also be represented in the normal mode representation. In the normal mode representation, the displacement field operator $\hat{\mathbf{D}}_{\perp}(\mathbf{r})$ reads

$$\hat{\mathbf{D}}_{\perp}(\mathbf{r}) = \hat{\mathbf{D}}(\mathbf{r}) = \sum_{k\lambda} iD_k \left[\hat{a}_{k\lambda} \mathbf{f}_{k\lambda}(\mathbf{r}) - \hat{a}_{k\lambda}^{\dagger} \mathbf{f}_{k\lambda}^*(\mathbf{r}) \right]. \quad (7)$$

Here, $D_k = \sqrt{\hbar\omega_k \varepsilon_0 / 2}$, where ω_k denotes the photonic frequency, and $\hat{a}_{k\lambda}^{\dagger}$ ($\hat{a}_{k\lambda}$) denotes the creation (annihilation) operator of the photon mode. In Eq. (2), the magnetic field operator is given by $\hat{\mathbf{B}}(\mathbf{r}) = \frac{1}{\sqrt{\varepsilon_0}} \nabla \times \hat{\mathbf{A}}(\mathbf{r})$.

Here, the vector potential $\hat{\mathbf{A}}(\mathbf{r})$ is

$$\hat{\mathbf{A}}_{\perp}(\mathbf{r}) = \sum_{k\lambda} A_k \left[\hat{a}_{k\lambda} \mathbf{f}_{k\lambda}(\mathbf{r}) + \hat{a}_{k\lambda}^{\dagger} \mathbf{f}_{k\lambda}^*(\mathbf{r}) \right], \quad (8)$$

where $A_k = \sqrt{\hbar/2\omega_k \varepsilon_0}$. Hence, in the normal mode representation, the photonic Hamiltonian in Eq. (2) can be expressed as

$$\hat{H}_{\text{ph}} = \sum_{k\lambda} \hbar\omega_k \hat{a}_{k\lambda}^{\dagger} \hat{a}_{k\lambda}. \quad (9)$$

Given a collection of N charge-neutral molecules, let $\hat{\boldsymbol{\mu}}^{(n)}$ be the molecular dipole operator of the n -th

molecule. The polarization density operator $\hat{\mathcal{P}}(\mathbf{r})$ in Eq. (5) can be rewritten as

$$\hat{\mathcal{P}}(\mathbf{r}) = \sum_{n=1}^N \hat{\boldsymbol{\mu}}^{(n)} \delta(\mathbf{r} - \mathbf{r}_n), \quad (10)$$

where \mathbf{r}_n denotes the position of the n -th molecule. When Eq. (10) is substituted into the light-matter interaction Hamiltonian defined in Eq. (3), \hat{H}_{int} becomes⁵²

$$\begin{aligned} \hat{H}_{\text{int}} = & - \sum_{k\lambda} \sum_{n=1}^N iD_k \left[\hat{a}_{k\lambda} \mathbf{f}_{k\lambda}(\mathbf{r}_n) - \hat{a}_{k\lambda}^\dagger \mathbf{f}_{k\lambda}^*(\mathbf{r}_n) \right] \cdot \hat{\boldsymbol{\mu}}^{(n)} \\ & + \sum_{k\lambda} \frac{1}{2\epsilon_0} \left| \sum_{n=1}^N \hat{\boldsymbol{\mu}}^{(n)} \cdot \mathbf{f}_{k\lambda}(\mathbf{r}_n) \right|^2. \end{aligned} \quad (11)$$

To proceed, we further rewrite $\hat{a}_{k\lambda}$ and $\hat{a}_{k\lambda}^\dagger$ as $\hat{p}_{k\lambda}$ and $\hat{q}_{k\lambda}$:

$$\hat{a}_{k\lambda} = \frac{1}{\sqrt{2\hbar\omega_k}} (\omega_k \hat{q}_{k\lambda} + i\hat{p}_{k\lambda}), \quad (12a)$$

$$\hat{a}_{k\lambda}^\dagger = \frac{1}{\sqrt{2\hbar\omega_k}} (\omega_k \hat{q}_{k\lambda} - i\hat{p}_{k\lambda}). \quad (12b)$$

When Eq. (12) is substituted into \hat{H}_{ph} in Eq. (9) as well as \hat{H}_{int} in Eq. (11), the field-related Hamiltonian $\hat{H}_{\text{F}} \equiv \hat{H}_{\text{ph}} + \hat{H}_{\text{int}}$ can be expressed as:

$$\begin{aligned} \hat{H}_{\text{F}} = & \sum_{k\lambda} \frac{1}{2} \omega_k^2 \left(\hat{q}_{k\lambda} - \sum_{n=1}^N \frac{\hat{\boldsymbol{\mu}}^{(n)}}{\sqrt{\epsilon_0 \omega_k}} \cdot \text{Im}[\mathbf{f}_{k\lambda}(\mathbf{r}_n)] \right)^2 \\ & + \frac{1}{2} \left(\hat{p}_{k\lambda} - \sum_{n=1}^N \frac{\hat{\boldsymbol{\mu}}^{(n)}}{\sqrt{\epsilon_0}} \cdot \text{Re}[\mathbf{f}_{k\lambda}(\mathbf{r}_n)] \right)^2. \end{aligned} \quad (13)$$

At this point, we assume that $\mathbf{f}_{k\lambda}(\mathbf{r}_n)$ is always real-valued, so $\text{Im}[\mathbf{f}_{k\lambda}(\mathbf{r}_n)] \equiv 0$ and only $\hat{p}_{k\lambda}$ is coupled to the molecules. Because photons are harmonic oscillators, we may also exchange $\hat{p}_{k\lambda}$ and $\hat{q}_{k\lambda}$ in Eq. (13). Practically speaking, we may redefine $\hat{p}'_{k\lambda} = \omega_k \hat{q}_{k\lambda}$ and $\hat{q}'_{k\lambda} = -\frac{1}{\omega_k} \hat{p}_{k\lambda}$. After this exchange, the canonical commutation relation is preserved: $[\hat{p}'_{k\lambda}, \hat{q}'_{k\lambda}] = [\hat{p}_{k\lambda}, \hat{q}_{k\lambda}] = i\hbar$, and the Hamiltonian becomes:

$$\hat{H}_{\text{F}} = \sum_{k\lambda} \frac{1}{2} \hat{p}_{k\lambda}^2 + \frac{1}{2} \omega_k^2 \left(\hat{q}_{k\lambda} + \sum_{n=1}^N \frac{\hat{\boldsymbol{\mu}}^{(n)} \cdot \mathbf{f}_{k\lambda}(\mathbf{r}_n)}{\sqrt{\epsilon_0 \omega_k}} \right)^2. \quad (14)$$

Eq. (14) can be regarded as a generalized, multi-mode form of the widely used single-mode Pauli-Fierz Hamiltonian.

2. Toward molecular dynamics simulations

To be suitable for molecular dynamics simulations, the quantum position and momentum operators of photons

are rescaled as

$$\hat{p}_{k\lambda} = \tilde{\hat{p}}_{k\lambda} / \sqrt{m_{k\lambda}}, \quad (15a)$$

$$\hat{q}_{k\lambda} = \tilde{\hat{q}}_{k\lambda} \sqrt{m_{k\lambda}}, \quad (15b)$$

where $m_{k\lambda}$ denotes the auxiliary mass of the photon mode, which is introduced to make the photonic dynamics compatible with conventional molecular dynamics packages. With this rescaling, the field-related Hamiltonian in Eq. (14) becomes

$$\begin{aligned} \hat{H}_{\text{F}} = & \sum_{k\lambda} \frac{1}{2m_{k\lambda}} \tilde{\hat{p}}_{k\lambda}^2 \\ & + \frac{1}{2} m_{k\lambda} \omega_k^2 \left(\tilde{\hat{q}}_{k\lambda} + \sum_{n=1}^N \frac{\hat{\boldsymbol{\mu}}^{(n)} \cdot \mathbf{f}_{k\lambda}(\mathbf{r}_n)}{\sqrt{\epsilon_0 m_{k\lambda} \omega_k}} \right)^2. \end{aligned} \quad (16)$$

Finally, we project the QED Hamiltonian in Eq. (16) to the electronic ground state. Under this cavity Born-Oppenheimer approximation,⁵³ the light-matter Hamiltonian becomes

$$\hat{H}_{\text{QED}}^{\text{G}} = \hat{H}_{\text{M}}^{\text{G}} + \hat{H}_{\text{F}}^{\text{G}}, \quad (17a)$$

where $\hat{H}_{\text{M}}^{\text{G}}$ denotes the conventional (kinetic + potential) molecular Hamiltonian in the electronic ground state, and the field-related Hamiltonian becomes

$$\begin{aligned} \hat{H}_{\text{F}}^{\text{G}} = & \sum_{k\lambda} \frac{1}{2m_{k\lambda}} \tilde{\hat{p}}_{k\lambda}^2 \\ & + \frac{1}{2} m_{k\lambda} \omega_k^2 \left(\tilde{\hat{q}}_{k\lambda} + \sum_{n=1}^N \frac{\hat{\boldsymbol{\mu}}_{\text{g}}^{(n)} \cdot \mathbf{f}_{k\lambda}(\mathbf{r}_n)}{\sqrt{\epsilon_0 m_{k\lambda} \omega_k}} \right)^2. \end{aligned} \quad (17b)$$

Here, $\hat{\boldsymbol{\mu}}_{\text{g}}^{(n)}$ denotes the dipole operator of the n -th molecule under electronic ground state.

The electronic ground-state light-matter Hamiltonian in Eq. (17) resembles the Hamiltonian in Ref. 33. The only difference is that here the long wave approximation is not used and the spatial dependence of the photonic mode functions is explicitly considered. If the long wave approximation is taken here, $\mathbf{f}_{k\lambda}(\mathbf{r}_n) \equiv \boldsymbol{\xi}_{\lambda} / \sqrt{\Omega}$ (i.e., there is no spatial variance in the photonic mode functions), Eq. (17) is reduced to the light-matter Hamiltonian in Ref. 33.

B. Efficient mesoscale CavMD simulations

After obtaining the generalized light-matter Hamiltonian in Eq. (17), we are interested in deriving an efficient simulation scheme of CavMD.

1. A brute-force approach

Given the quantum Hamiltonian in Eq. (17), the classical equations of motion of the coupled light-matter sys-

tem become

$$M_\alpha \ddot{\mathbf{R}}_\alpha = \mathbf{F}_\alpha^{(0)} + \mathbf{F}_\alpha^{\text{cav}}, \quad (18a)$$

$$m_{k\lambda} \ddot{q}_{k\lambda} = -m_{k\lambda} \omega_k^2 \tilde{q}_{k\lambda} - \varepsilon_{k\lambda} d_{g,k\lambda}. \quad (18b)$$

Here, $d_{g,k\lambda}$ denotes the total molecular dipole moment projected along the cavity polarization direction:

$$d_{g,k\lambda} \equiv \sum_{n=1}^N \sqrt{\mathcal{V}} \boldsymbol{\mu}_g^{(n)} \cdot \mathbf{f}_{k\lambda}(\mathbf{r}_n), \quad (18c)$$

where \mathcal{V} , in the units of volume, denotes the normalization coefficient of the mode function which satisfies $\langle \mathcal{V} | \mathbf{f}_{k\lambda}(\mathbf{r}) |^2 \rangle = 1$. This normalization guarantees $\sqrt{\mathcal{V}} \mathbf{f}_{k\lambda}(\mathbf{r}_n)$ to be dimensionless, so $d_{g,k\lambda}$ maintains the same units as $\boldsymbol{\mu}_g^{(n)}$. M_α and \mathbf{R}_α denote the mass and position of the α -th nucleus, $\mathbf{F}_\alpha^{(0)}$ denotes the nuclear force acting on the α -th nucleus without the cavity (i.e., the same force as that in conventional molecular dynamics simulations), and $\mathbf{F}_\alpha^{\text{cav}}$ denotes the force from the cavity acting on the the α -th nucleus:

$$\mathbf{F}_\alpha^{\text{cav}} = - \sum_{k\lambda} \left(\varepsilon_{k\lambda} \tilde{q}_{k\lambda} + \frac{\varepsilon_{k\lambda}^2}{m_{k\lambda} \omega_k^2} d_{g,k\lambda} \right) \frac{\partial d_{g,k\lambda}}{\partial \mathbf{R}_\alpha}, \quad (19)$$

where the effective light-matter coupling $\varepsilon_{k\lambda}$ is defined as

$$\varepsilon_{k\lambda} \equiv \sqrt{\frac{m_{k\lambda} \omega_k^2}{\mathcal{V} \varepsilon_0}}. \quad (20)$$

Because the dielectric boundary conditions determine the photonic mode functions, given an explicit form of $\mathbf{f}_{k\lambda}(\mathbf{r}_n)$, Eq. (18) allows for directly propagating the coupled photon-molecular dynamics in the dielectric environment. However, due to the large number of molecules and the infinite number of photonic modes involved in planar Fabry-Pérot cavities, a brute-force propagation of Eq. (18) is unrealistic.

Below, using a rectangular parallelepiped as the photonic boundary conditions, we demonstrate how to efficiently simulate CavMD in the mesoscale with an affordable computational cost.

2. Photonic mode functions in a rectangular parallelepiped

For a rectangular parallelepiped shown in Fig. 1, the photonic mode functions are⁵⁴

$$f_{k,x} = \sqrt{\frac{8}{\Omega}} \cos(k_x x) \sin(k_y y) \sin(k_z z), \quad (21a)$$

$$f_{k,y} = \sqrt{\frac{8}{\Omega}} \sin(k_x x) \cos(k_y y) \sin(k_z z), \quad (21b)$$

$$f_{k,z} = \sqrt{\frac{8}{\Omega}} \sin(k_x x) \sin(k_y y) \cos(k_z z). \quad (21c)$$

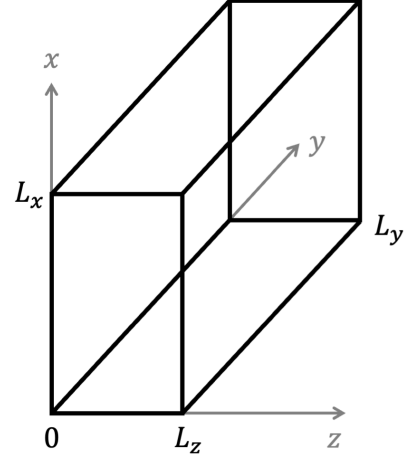


FIG. 1. An optical resonator with volume Ω shaped as a rectangular parallelepiped, with lengths along the three dimensions denoted as L_x , L_y , and L_z . The electric field amplitude is assumed to be zero at the boundaries.

Here, Ω denotes the volume of the rectangular parallelepiped;

$$k_x = \frac{l_x \pi}{L_x}, \quad (22a)$$

$$k_y = \frac{l_y \pi}{L_y}, \quad (22b)$$

$$k_z = \frac{l_z \pi}{L_z}, \quad (22c)$$

where L_x , L_y , and L_z denote the lengths of the rectangular parallelepiped in three dimensions, and l_x , l_y , and l_z are independent integers.

This rectangular parallelepiped can be used to simulate CavMD dynamics in planar Fabry-Pérot cavities. To this end, we assume the cavity is placed along the z direction and $L_z \ll L_x, L_y$. If only the fundamental cavity mode of k_z is relevant to our research interest (e.g., when the high-frequency vibrational mode of molecules is near resonant with the fundamental cavity mode), we can further take $k_z = \pi/L_z$ and ignore any higher order modes. If the molecules are placed near the plane of $z = L_z/2$ (as demonstrated in Fig. 2a), only the following mode functions have a non-zero contribution:

$$f_{k,x} = \sqrt{\frac{8}{\Omega}} \cos(k_x x) \sin(k_y y), \quad (23a)$$

$$f_{k,y} = \sqrt{\frac{8}{\Omega}} \sin(k_x x) \cos(k_y y). \quad (23b)$$

For this simplified cavity setup, the normalization coefficient $\mathcal{V} = \Omega/2$, so $\langle \mathcal{V} | f_{k,x} |^2 \rangle = \langle \mathcal{V} | f_{k,y} |^2 \rangle = 1$. The corresponding cavity mode frequency ω_k becomes

$$\omega_k = c \sqrt{\left(\frac{\pi}{L_z} \right)^2 + k_{\parallel}^2}. \quad (24)$$

Here, $c = c_0/n_{\text{ref}}$ denotes the speed of light in the medium; c_0 denotes the speed of light in the vacuum and n_{ref} denotes the refractive index of the medium. The in-plane wave vector k_{\parallel} is defined as

$$k_{\parallel}^2 = \left(\frac{l_x \pi}{L_x}\right)^2 + \left(\frac{l_y \pi}{L_y}\right)^2. \quad (25)$$

In practice, we include a finite number of cavity modes with $1 \leq l_x \leq l_x^{\text{max}}$ and $1 \leq l_y \leq l_y^{\text{max}}$.

3. A 2D grid of molecules

Although we have assumed that the molecules of interest are confined to a thin layer along the plane $z = L_z/2$ (Fig. 2a), directly simulating all N molecules in this layer is computationally expensive. Thus, we approximate the full molecular system by a smaller number of grid points (Fig. 2c), where each grid point represents a finite-sized, explicitly simulated molecular system. This grid representation allows us to simulate the system with bearable computational resources.

With the 2D grid representation, the total molecular dipole $d_{g,k\lambda}$ defined in Eq. (18c) can be calculated as

$$d_{g,k\lambda} = N_{\text{ratio}} d_{g,k\lambda}^{\text{sub}}. \quad (26)$$

Here, N_{ratio} denotes the ratio between the true number of molecules in the cavity versus the number of explicitly simulated molecules; $d_{g,k\lambda}^{\text{sub}}$ denotes the total dipole moment of the explicitly simulated molecules (the purple areas in Fig. 2c),

$$d_{g,k\lambda}^{\text{sub}} = \sum_{\vec{n}=(n_x, n_y)} \sqrt{\mathcal{V}} \boldsymbol{\mu}_g^{(\vec{n})} \cdot \mathbf{f}_{k\lambda}(\mathbf{r}_{\vec{n}}), \quad (27)$$

where $\boldsymbol{\mu}_g^{(\vec{n})}$ denotes the total molecular dipole in each explicitly simulated grid point, and $\mathbf{r}_{\vec{n}}$ denotes the position of each grid point labeled by $\vec{n} = (n_x, n_y)$.

4. A practical classical simulation scheme

With the molecular dipole defined above, we can rewrite the equations of motion in Eq. (18) as

$$M_{\alpha} \ddot{\mathbf{R}}_{\alpha} = \mathbf{F}_{\alpha}^{(0)} + \mathbf{F}_{\alpha}^{\text{cav}}, \quad (28a)$$

$$m_{k\lambda} \ddot{\tilde{q}}_{k\lambda} = -m_{k\lambda} \omega_k^2 \tilde{q}_{k\lambda} - \tilde{\varepsilon}_{k\lambda} d_{g,k\lambda}^{\text{sub}}, \quad (28b)$$

where the cavity force is

$$\mathbf{F}_{\alpha}^{\text{cav}} = - \sum_{k\lambda} \left(\tilde{\varepsilon}_{k\lambda} \tilde{q}_{k\lambda} + \frac{\tilde{\varepsilon}_{k\lambda}^2}{m_{k\lambda} \omega_k^2} d_{g,k\lambda}^{\text{sub}} \right) \frac{\partial d_{g,k\lambda}^{\text{sub}}}{\partial \mathbf{R}_{\alpha}}. \quad (28c)$$

Here, we have defined the rescaled photon position $\tilde{q}_{k\lambda}$ as

$$\tilde{q}_{k\lambda} \equiv \tilde{q}_{k\lambda} / \sqrt{N_{\text{ratio}}} \quad (29)$$

and the new effective light-matter coupling as

$$\tilde{\varepsilon}_{k\lambda} = \sqrt{N_{\text{ratio}}} \varepsilon_{k\lambda} = \sqrt{\frac{N_{\text{ratio}} m_{k\lambda} \omega_k^2}{\mathcal{V} \epsilon_0}}. \quad (30)$$

The rescaling introduced in Eqs. (29) and (30) is necessary because it guarantees that the equations of motion in Eq. (28) are of the same form as Eq. (18), except that (i) the total dipole moment of the explicitly simulated molecules $d_{g,k\lambda}^{\text{sub}}$ replaces the true total dipole moment of the whole molecular layer and (ii) $\tilde{\varepsilon}_{k\lambda}$ becomes unphysically large. Of course, as demonstrated in previous CavMD work^{47,49,55}, because of the potential for artifacts introduced by this rescaling procedure, it is necessary to validate whether the simulated cavity effects can persist in real experiments containing a macroscopic number of molecules. This validation process can be done by increasing the number of explicitly simulated molecules as well as reducing $\tilde{\varepsilon}_{k\lambda}$ (these two parameters should be changed in a manner such that the observed Rabi splitting remains the same) until the convergence of the simulation results.

Eq. (28) illustrates that three molecular quantities, i.e., $\mathbf{F}_{\alpha}^{(0)}$, $d_{g,k\lambda}^{\text{sub}}$, and $\partial d_{g,k\lambda}^{\text{sub}} / \partial \mathbf{R}_{\alpha}$, must be determined during CavMD simulations. Previously, under the single-mode limit, these three quantities have been evaluated using both non-polarizable empirical force fields³³ and hybrid QM/MM calculations⁵⁰.

When non-polarizable force fields are used to describe the molecules, the total dipole moment of the molecular system at each grid point $\vec{n} = (n_x, n_y)$ becomes

$$\boldsymbol{\mu}_g^{(\vec{n})} = \sum_{\alpha \in \vec{n}} Q_{\alpha} \mathbf{R}_{\alpha}, \quad (31)$$

where Q_{α} denotes the partial charge of the α -th nucleus. Therefore, according to Eq. (27), $d_{g,k\lambda}^{\text{sub}}$ can be expressed as

$$d_{g,k\lambda}^{\text{sub}} = \sum_{\vec{n}} \sum_{\alpha \in \vec{n}} \sqrt{\mathcal{V}} Q_{\alpha} \mathbf{R}_{\alpha} \cdot \mathbf{f}_{k\lambda}(\mathbf{r}_{\vec{n}}). \quad (32)$$

Similarly, the dipole derivatives become

$$\frac{\partial d_{g,k\lambda}^{\text{sub}}}{\partial R_{\alpha i}^{(\vec{n})}} = \sqrt{\mathcal{V}} Q_{\alpha} \mathbf{e}_i \cdot \mathbf{f}_{k\lambda}(\mathbf{r}_{\vec{n}}), \quad (33)$$

where $R_{\alpha i}^{(\vec{n})}$ represents the nuclear position along the i -th direction at grid point $\vec{n} = (n_x, n_y)$, and \mathbf{e}_i denotes the unit vector along the i -th direction. When the equations for the dipole and its derivatives [Eqs. (32) and (33)] are substituted into the equations of motion [Eq. (28)], the mesoscale cavity dynamics can be efficiently simulated.

Recent studies suggest that the dipole self-energy term in the light-matter Hamiltonian can be important and may induce additional intermolecular interactions.⁵⁶⁻⁵⁸ As a dynamics approach, CavMD includes the dipole self-energy term and evaluates its gradients on-the-fly,

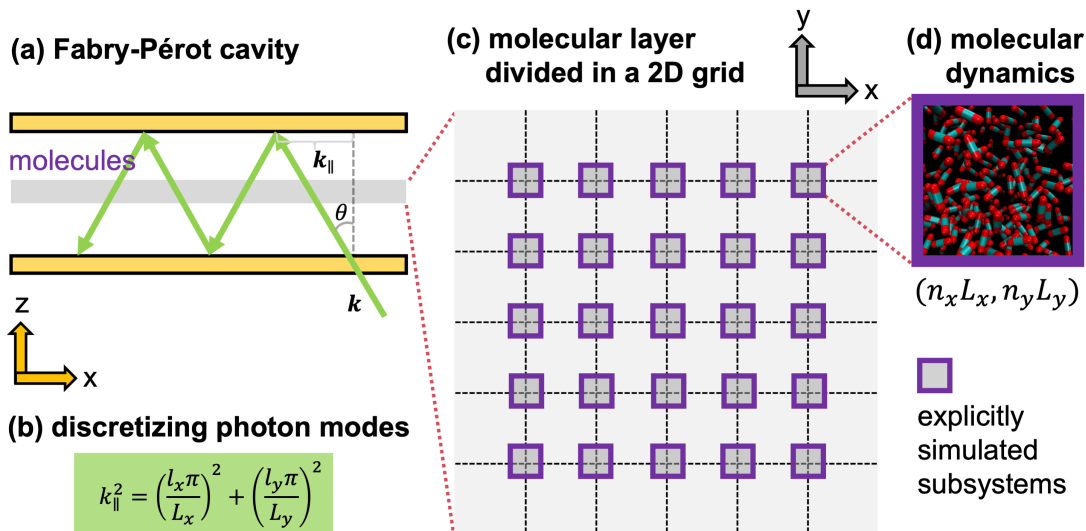


FIG. 2. Strategy for simulating Fabry-Pérot vibrational strong coupling. (a) The Fabry-Pérot cavity viewed in the xz plane. A layer of molecules is confined at the middle of the cavity. (b) A finite number of photon modes are simulated by discretizing k_{\parallel} . (c) The molecules are divided in a 2D grid along the xy plane. (d) For an efficient simulation of the macroscopic molecular system, only the small molecular subsystems at different grid points (labeled as the purple squares) are explicitly simulated.

which contain dipole moments and their derivatives. Of course, because dipole moments and their derivatives are important, a more accurate description of strong coupling may require a dipole surface beyond the use of fixed point charges, e.g., using inputs from on-the-fly electronic structure theory or machine-learning dipole surfaces. Nevertheless, previous work has demonstrated that using fixed point charges to represent the dipole surface can yield polariton relaxation dynamics in qualitative agreement with experiments.^{46,47}

As a side note, the current formalism of CavMD can be directly applied to study systems with well-defined, charge-neutral molecules. For this type of the systems, the dipole moment per grid point, $\mu_{\mathbf{g}}^{(\vec{n})}$, is independent of periodic boundary conditions (applied in each molecular subsystem) and the origin of the coordinate system. In other words, $\mu_{\mathbf{g}}^{(\vec{n})}$ for well-defined, charge-neutral molecules is translational invariant. However, when the molecular subsystems contain free ions, extra care is needed when performing CavMD simulations. Because $\mu_{\mathbf{g}}^{(\vec{n})}$ for free ions is translational variant (depending on periodic boundary conditions and the origin of the coordinate system), the translational motion of free ions may potentially contaminate the photonic dynamics through the light-matter coupling in Eq. (14). One possible solution is to remove the free ion contribution when evaluating $\mu_{\mathbf{g}}^{(\vec{n})}$ in Eq. (31), thus ensuring the translationally invariant dipole moments. More extensive study is needed to explore the proper CavMD scheme for simulating molecular systems with free ions.

5. An outline of mesoscale CavMD simulation

Here, we give a brief outline on how to perform mesoscale CavMD simulations from scratch.

- (i) Determine the cavity mode structure by setting the fundamental cavity frequency $\omega_{\perp} = c\pi/L_z$, cavity mirror plane lengths L_x, L_y , as well as the maximal mode numbers l_x^{\max}, l_y^{\max} along the cavity mirror plane [Eqs. (23)-(25)].
- (ii) Determine the number and positions of molecular grid points along the (x, y) plane, and setup the initial molecular geometry for each grid point [Eqs. (31)-(33)].
- (iii) Given the effective light-matter coupling $\tilde{\varepsilon}_{k\lambda}$, run the mesoscale CavMD simulation using Eq. (28).
- (iv) (Optional) Increase the explicitly simulated molecular number N_{simu} (which depends on both N_{grid} and the number of molecules in each grid point) while reducing the effective coupling strength $\tilde{\varepsilon}_{k\lambda} \propto 1/\sqrt{N_{\text{simu}}}$ accordingly, and then check whether the observed cavity effect is robust for different cavity sizes. The large N_{simu} limit may correspond to VSC in realistic planar Fabry-Pérot cavities.

6. Connecting to previous CavMD work with a single cavity mode

The present formalism can be reduced to previous CavMD work with only a single cavity mode, which contains two degenerate cavity photons polarized along ei-

ther the x - or the y -direction.³³ This reduction is guaranteed because the equations of motion derived in Eq. (28) are identical to those of our earlier work.^{33,47}

In detail, to include only two degenerate cavity photons which are polarized along either the x or the y direction, we set $k_x = \pi/L_x$, $k_y = \pi/L_y$, and $L_x = L_y \gg L_z$. Then, we may use only a single grid point to represent the whole molecular system, where the location of the grid point is denoted $x = \frac{L_x}{4}$ and $y = \frac{L_y}{4}$. With these parameters, both $k_x x$ and $k_y y$ equal $\pi/4$; according to Eq. (23), the two possible photon mode functions become

$$f_{k,x} = \sqrt{\frac{2}{\Omega}} = \sqrt{\frac{1}{\mathcal{V}}}, \quad (34a)$$

$$f_{k,y} = \sqrt{\frac{2}{\Omega}} = \sqrt{\frac{1}{\mathcal{V}}}. \quad (34b)$$

With the above parameters, the molecular dipole and its derivatives [Eqs. (32) and (33)] become

$$d_{g,k\lambda}^{\text{sub}} = \sum_{\alpha} Q_{\alpha} \mathbf{R}_{\alpha} \cdot \boldsymbol{\xi}_{\lambda}, \quad (35a)$$

and

$$\frac{\partial d_{g,k\lambda}^{\text{sub}}}{\partial R_{\alpha i}} = Q_{\alpha} \mathbf{e}_i \cdot \boldsymbol{\xi}_{\lambda}, \quad (35b)$$

which are identical to previous work.³³ Hence, the current implementation is consistent with previous CavMD work with a single cavity mode.

7. Path-integral simulations of nuclear and photonic quantum effects

Before ending this section, we briefly discuss how to include quantum effects in mesoscale CavMD simulations. Although the above equations of motion in Eq. (28) are classical, nuclear and photonic quantum effects can also be captured by performing path-integral simulations.^{44,45} After all, in Eq. (28), photons behave just like additional ‘‘nuclei’’. Hence, one can directly apply different flavors of path-integral approaches developed over the past decades⁵⁹ to study VSC.

III. SIMULATION DETAILS

We implemented the mesoscale CavMD scheme in the open source package i-PI;⁶⁰ see the caption of Fig. 3 for a detailed description of the implementation. In particular, the forces of molecular systems at different grid points were evaluated in parallel by i-PI through the socket interface by connecting to multiple clients; each client runs its own force evaluation code. The code and input files are available on Github at <https://github.com/TaoELi/cavity-md-ipi>.

The implementation of our method was tested on various cavity setups. The sketch of these cavity setups and the corresponding parameters are shown in Fig. (4) and Table I. In each cavity setup, the whole molecular system was represented by N_{grid} grid points. In cavity #1-#4, because the grid points along the y -direction all located at the origin ($y = 0$), as shown in Eq. (23), the mode functions along the x -direction vanished. In other words, in cavity #1-#4, cavity modes polarized along the x -direction were decoupled from the molecules. Throughout the paper, the cavity loss is set as zero. The method and results for including the cavity loss are briefly discussed in the Appendix. The auxiliary mass of the photon modes is set to $m_c = m_{l\lambda} = 1$ a.u.

Each grid point was assigned a periodic boundary condition box containing 36 CO₂ molecules, which were explicitly simulated. The molecular density of the box was set to 1.101 g/cm³. The CO₂ molecules were modeled with the same force field that was used in previous work, which has been validated against experimental data.⁴⁷ Intermolecular Coulombic interactions were calculated using Ewald summation.

For equilibrium classical simulations, the coupled cavity-molecular system was initially equilibrated for 20 ps under an NVT ensemble at 300 K, using a time step of 0.5 fs. A Langevin thermostat with a friction lifetime of 100 fs was attached to each particle (both photons and nuclei). After this equilibration simulation, 40 consecutive 20-ps NVE simulations were performed using a time step of 0.5 fs. At the beginning of each NVE simulation, the initial velocities of all particles were re-sampled with a Maxwell-Boltzmann distribution at 300 K. For nonequilibrium classical simulation of polariton-polariton scattering in cavity #1, given the 40 starting geometries of the above consecutive NVE simulation, the photonic energy of the $l_x = 12$ cavity mode was reset to 195 quanta. In practice, this initial excitation was implemented by setting the y -coordinate of the $l_x = 12$ cavity mode to $y_c = 100$ Å, according to $\frac{1}{2}m_c\omega_c^2 y_c^2 = 195 \hbar\omega_c$. With each of these perturbed geometries, a 20-ps NVE simulation was performed.

For equilibrium path integral simulations, the thermostatted ring polymer molecular dynamics (TRPMD) approach was used.⁶¹ While the simulation conditions of TRPMD largely resembled the classical case, here the difference is highlighted. We initialized the ring polymer with 4 beads for all nuclei and cavity photons with a time step of 0.25 fs. During all TRPMD simulations, a path integral Langevin equation (PILE) thermostat⁶¹ was attached to the internal modes of the ring polymer with an optimally damped coefficient $\lambda = 1/2$.

Outside the cavity, the IR spectrum of liquid CO₂ was calculated by Fourier transforming the dipole autocorrelation function of the molecules:^{47,62-65}

$$F(\omega) \propto \omega^2 \int_{-\infty}^{+\infty} dt e^{-i\omega t} \left\langle \sum_{i=x,y,z} \mu_i(0) \mu_i(t) \right\rangle. \quad (36)$$

Here, $\mu_i(t)$ denotes the total dipole moment of the molec-

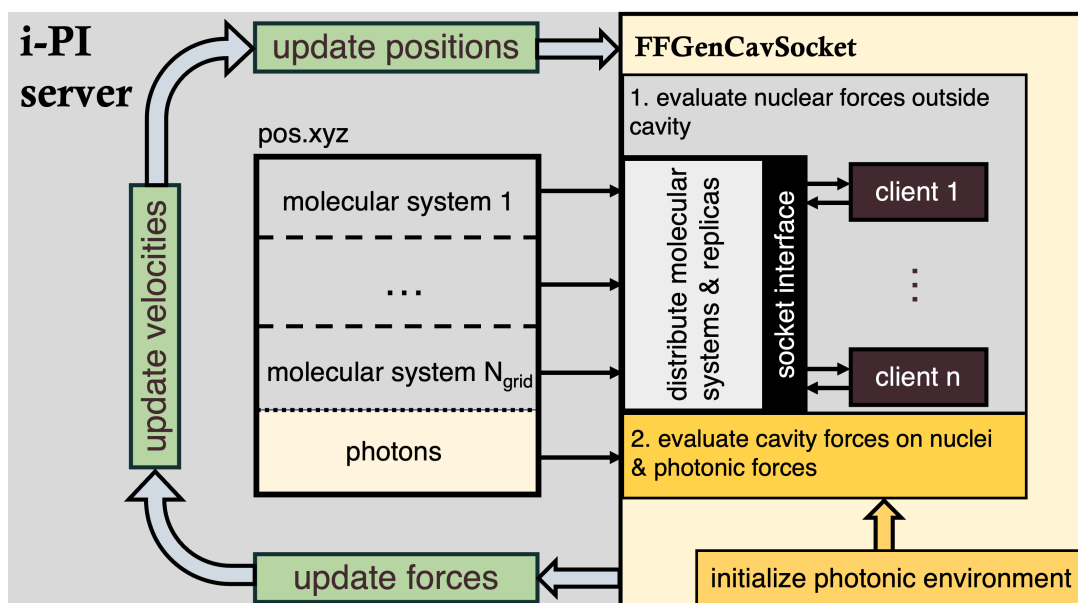


FIG. 3. A sketch of the mesoscale CavMD scheme as implemented in i-PI. The original i-PI server is responsible for updating the positions and velocities of the entire molecular + photonic system. The newly implemented **FFGenCavSocket** method, which stands for the **force field socket** interface for a **general cavity** setup, evaluates the forces for the whole system, including both the nuclear forces at different grid points (as shown in Fig. 2c) and the photonic forces. In path-integral simulations with P beads, the **FFGenCavSocket** method can connect to $N_{\text{grid}} \times P$ different clients in parallel, thus significantly reducing the gradient evaluation time.



FIG. 4. Sketch of different cavity setups. Cavity #0 represents the standard cavity setup in previous CavMD simulations, where a large ensemble of molecules is coupled to a single cavity mode. Cavity #1-#5 represent the five cavity setups simulated in this work; see Table I for the corresponding cavity parameters.

TABLE I. Parameters for different cavity setups. In the table, $\Delta\omega_{x,y} = c\pi/L_{x,y}$; $\Delta\omega_y = 0$ indicates $L_y = \infty$. Each array along the x - or y -direction represents the evenly spaced locations (in the units of L_x or L_y) of the molecular grid points along the corresponding axis. For example, in cavity #1, $[0.027, 0.054, \dots, 0.973]$ represent the x -grid locations for $N_{\text{grid}} = 36$ grid points. At each grid point, 36 CO_2 molecules are explicitly simulated under periodic boundary conditions. Cavity #1-#4 represent four sets of parameters for 1D cavities, while cavity #5 simulates a 2D cavity. The effective coupling strength $\tilde{\epsilon}$ refers to $\tilde{\epsilon}_{k\lambda}(\omega_{\perp})$, as $\tilde{\epsilon}_{k\lambda}$ is proportional to ω_k [Eq. (30)].

cavity	ω_{\perp} [cm ⁻¹]	$\Delta\omega_x$ [cm ⁻¹]	$\Delta\omega_y$ [cm ⁻¹]	l_x^{max}	l_y^{max}	N_{grid}	x grid positions [L_x]	y grid positions [L_y]	$\tilde{\epsilon}$ [a.u.]
#1	2320	50	0	36	1	36	[0.027, 0.054, ..., 0.973]	[0.0]	5×10^{-5}
#2	2320	16.67	0	108	1	36	[0.027, 0.054, ..., 0.973]	[0.0]	5×10^{-5}
#3	2320	50	0	36	1	6	[0.143, 0.286, ..., 0.857]	[0.0]	1.225×10^{-4}
#4	2320	50	0	36	1	36	[0.5, 0.5, ..., 0.5]	[0.0]	5×10^{-5}
#5	2320	50	50	18	18	1296	[0.027, 0.054, ..., 0.973]	[0.027, 0.054, ..., 0.973]	8.3×10^{-6}

ular system in each dimension.

Inside the cavity, the IR spectrum of the polaritons was calculated by evaluating the position autocorrelation function of the cavity photons:

$$F_{k\lambda}(\omega) \propto \omega^2 \int_{-\infty}^{+\infty} dt e^{-i\omega t} \langle \tilde{q}_{k\lambda}(0) \tilde{q}_{k\lambda}(t) \rangle. \quad (37)$$

IV. RESULTS

A. Cavity #1: An 1D approximation of planar Fabry-Pérot cavities

As shown in Fig. 4, cavity #1 contains 36 cavity modes as well as 36 evenly spaced grid points along the x direction. For such a 1D cavity setup, the cavity frequency dispersion relation reads

$$\omega_c(l_x) = \sqrt{\omega_{\perp}^2 + l_x^2 \Delta\omega_x^2}, \quad (38)$$

where $\omega_{\perp} = 2320$ cm⁻¹, $\Delta\omega_x = 50$ cm⁻¹, and $l_x = 1, 2, \dots, 36$.

1. Polariton spectrum: the validity of the single-mode approximation

Fig. 5a shows the polariton spectrum (yellow line) of CO_2 confined in this cavity, obtained from classical CavMD simulations. The yellow line represents the polariton spectrum formed between the asymmetric C=O stretch (black line) of liquid CO_2 and the cavity photon mode at normal incidence (vertical green line). This polariton spectrum is calculated by taking the Fourier transform of the coordinate autocorrelation function of the lowest-frequency cavity mode (with $l_x = 1$). If only a single cavity mode at $l_x = 1$ is included in the simulation, the resulting polariton spectrum (red line) is identical to that of the 36-mode cavity #1. This agreement shows the validity of using the single-mode approximation for describing the linear-response polariton spectrum: Cavity modes at different ω_{\parallel} values effectively do not interact with each other. Of course, for cavity #1, when the

coordinate autocorrelation functions of cavity modes at different ω_{\parallel} are evaluated, the well-known ω_{\parallel} -dependent UP and LP branches^{11,13} can be recovered, as shown in Fig. 5b.

The lower panel of Fig. 5 provides analogous results when a TRPMD simulation is performed. Compared with the classical results in the upper panel, both the polariton peaks and the C=O asymmetric stretch are slightly red-shifted. The broadening of the peaks, as suggested by Ref. 45, may be attributed to the artifacts in TRPMD rather than a real quantum effect. Since such artifacts have been removed in more recent developments of TRPMD outside the cavity,⁶⁶ simulating polaritons using more advanced path-integral approaches is worth exploring. Nevertheless, the path-integral simulation performed here showcases the compatibility of our mesoscale CavMD with path-integral molecular dynamics in the i-PI code, both of which require calling multiple clients to evaluate molecular parameters. Because there is no significant difference between the classical and TRPMD results, for the calculations below, only classical simulations will be performed.

2. Polariton-polariton scattering beyond the single-mode approximation

Fig. 6a elaborates further on the 36-mode simulation, when the cavity mode at $l_x = 12$ (corresponding to $\omega_c = 2396$ cm⁻¹) is strongly excited at $t = 0$. The red line plots the photon energy dynamics of this initially excited cavity mode, while the blue line plots the summed photon energy of the other cavity modes ($l_x \neq 12$). In general, the excited cavity photon relaxes to the ground state within 10 ps, and the other cavity modes absorb energy transiently up to $t = 5 \sim 10$ ps and then dissipate their energy at later times. Apart from the energy scattering to the other cavity modes, the relaxation of the $l_x = 12$ photon (polaritons) stems also from polariton energy transfer to the dark modes. Cavity loss does not play a role in the photon relaxation dynamics, as the cavity loss is set to zero during our simulations. Please note that since the photon excitation at $\omega_c = 2396$ cm⁻¹ is implemented by displacing the photon coordinate at

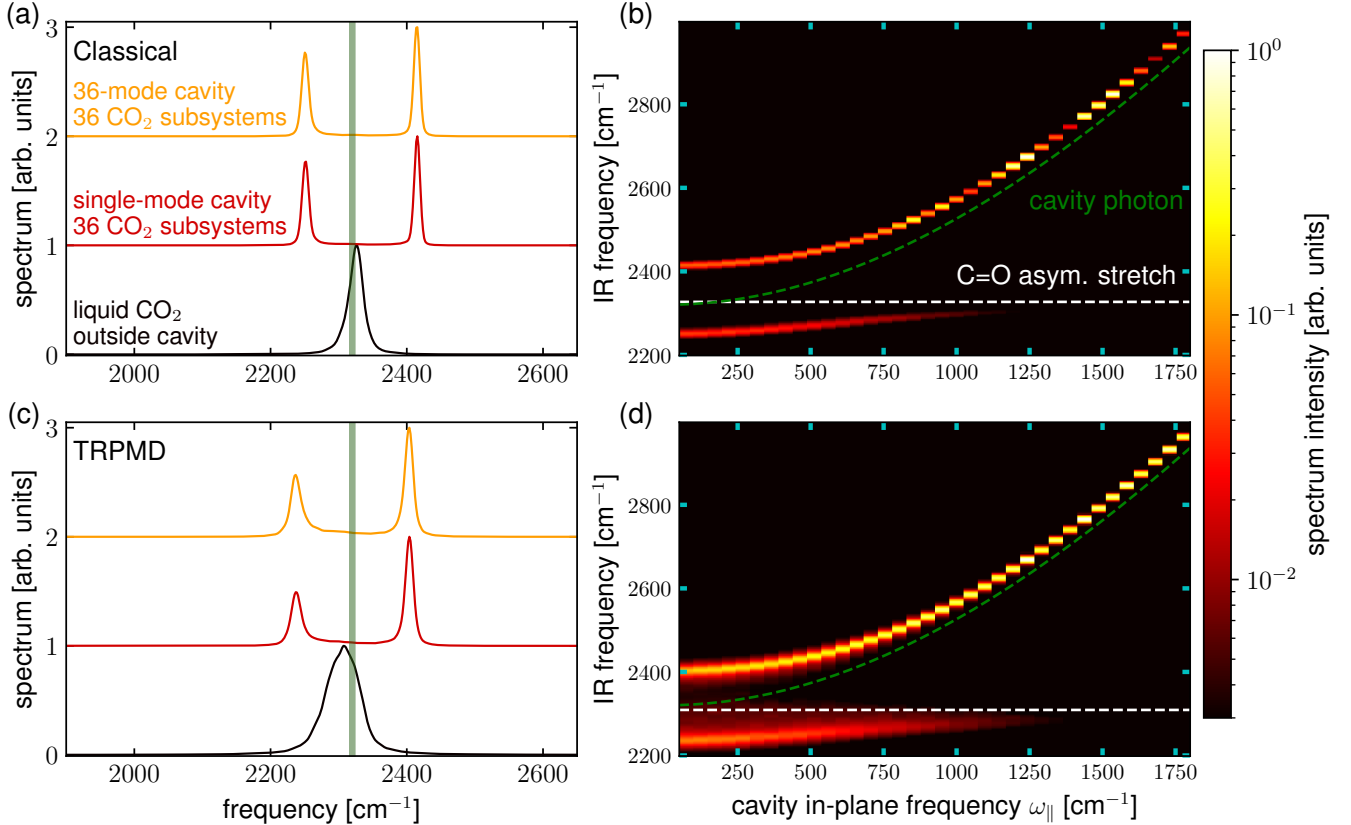


FIG. 5. Polariton spectra in a lossless cavity from classical (upper panel) or path-integral (bottom panel) CavMD simulations. (a) The normalized IR spectrum of liquid CO₂ outside the cavity (black), coupled to a single-mode cavity (red), or a multimode Fabry–Pérot-like 1D cavity (cavity #1, yellow). The vertical green line denotes the cavity frequency at normal incidence (the lowest-frequency cavity mode). (b) The polariton spectrum vs the cavity in-plane frequency ω_{\parallel} corresponding to the multimode cavity. (c, d) The same plot as the upper panel except that the TRPMD method is used to propagate the dynamics.

time $t = 0$, both the UP and LP have been equally excited. Such an initial excitation can be experimentally achieved by applying a short, wide-band pulse to equally excite both the UP and LP. Hence, the $l_x = 12$ excited photon mode exhibits a strong Rabi oscillation pattern initially ($t < 2$ ps). At later times, however, the Rabi oscillations disappear, as the LP lifetime is shorter than the UP lifetime;^{46,47} therefore, only the UP signal remains.

To better understand the dynamics of the remaining photon modes ($l_x \neq 12$), in Figs. 6b,c, we further provide the photon energy dynamics of each of these photon modes. Lines in yellow represent cavity modes with frequencies close to the initially excited photon frequency ($\omega_c = 2396$ cm⁻¹), and lines with deeper colors represent cavity modes with frequencies further from it. Clearly, among all of the remaining cavity modes, the closer the frequency to the initially excited photon mode, the more energy the initially unexcited cavity photon receives transiently. This frequency-dependent transient excitation indicates polariton-polariton scattering, a fundamental mechanism that has been widely studied both experimentally and theoretically in planar Fabry–Pérot cavities.³⁶ Because molecules interact with each other, interactions

among polaritons with different ω_{\parallel} values, which are hybrid light-matter states that can be viewed as molecular excitations modulated by cavity modes, can indeed occur. The polariton-polariton scattering process is unlikely to be mediated by the transiently excited molecular dark modes. This is because the excited dark modes are more likely to transfer energy to those polaritons with frequencies closer to the dark modes, a prediction which is contrary to what is observed in Figs. 6b,c.

As a short summary, although linear-response polariton spectra seem to suggest that the single-mode approximation is valid, nonequilibrium CavMD simulations emphasize that including ω_{\parallel} -dependent cavity modes is critical for accurately modeling the dynamics of polariton-polariton scattering events.

B. 1D Cavity setups which cannot be used to represent Fabry–Pérot cavities

The example of cavity #1 above represents a set of parameters that could be used to model realistic Fabry–Pérot cavities. However, it is also useful to investigate

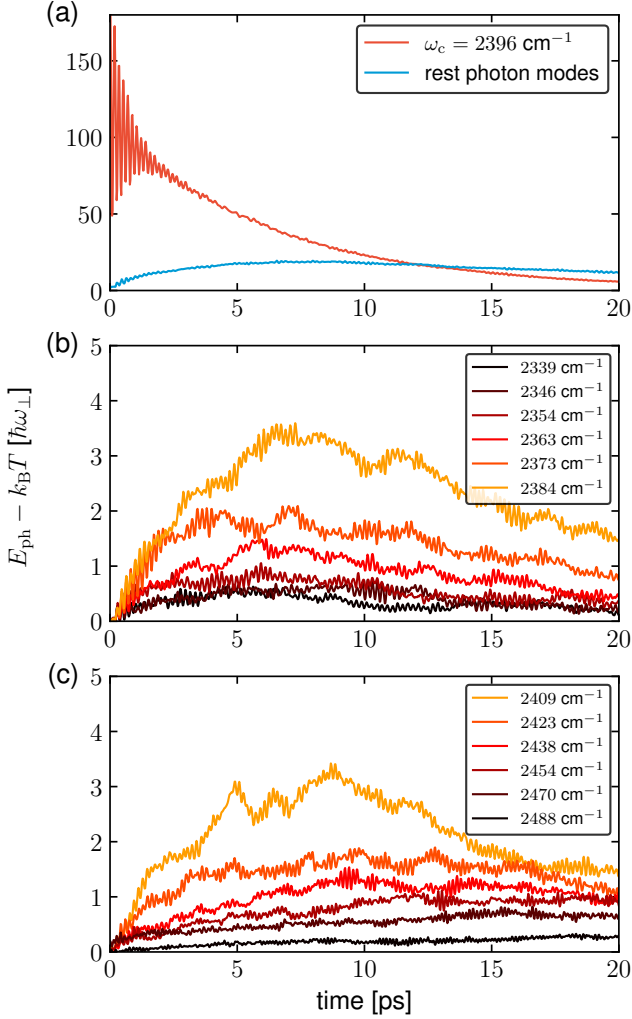


FIG. 6. Nonequilibrium photon energy dynamics in the cavity #1 setup when the cavity mode at $\omega_c = 2396 \text{ cm}^{-1}$ ($l_x = 12$) is initially excited. (a) Photon energy dynamics for the initially excited cavity mode (red line) vs. the summed photon energy of the remaining photon modes with $l_x \neq 12$ (blue line). (b,c) The photon energy dynamics for each individual cavity mode with frequency (b) $\omega_c < 2396 \text{ cm}^{-1}$ or (c) $\omega_c > 2396 \text{ cm}^{-1}$. Here, lines with yellow (black) colors represent cavity modes with frequencies close to (far from) the initially excited photon mode. Energy scattering occurs from the initially excited photon mode to the neighboring cavity modes at different ω_{\parallel} .

under which conditions the numerical scheme cannot be used to simulate realistic Fabry–Pérot cavities. To this end, we now consider such three additional sets of cavity parameters, labeled as cavity #2–#4.

1. Cavity #2

As shown in Table I, when compared to cavity #1, cavity #2 includes more cavity modes (108 instead of

36) and a smaller $\Delta\omega_x$ (16.67 cm^{-1} instead of 50 cm^{-1}). The physical meaning of reducing $\Delta\omega_x$ is demonstrated in Fig. 4: a larger L_x and a sparser distribution of the molecular grid points along the x -direction (the cavity mirror plane).

Fig. 7a plots the polariton spectrum at normal incidence (yellow line) for this 108-mode cavity. The polariton spectrum is red-shifted compared to the case when only the lowest-frequency cavity mode (with $l_x = 1$, red line) is included in the simulation. This difference indicates the breakdown of the single-mode approximation. More obviously, as shown in Fig. 7b, the ω_{\parallel} -dependent polariton spectrum exhibits a much more complicated polariton structure than Fig. 5b: here four polariton branches exist in the spectrum, with multiple avoided crossings.

2. Cavity #3

For another example, cavity #3 also resembles cavity #1 except here a smaller number of molecular grid points, 6 (instead of 36), are evenly distributed. In order to guarantee a similar Rabi splitting as cavity #1, the effective light-matter coupling $\tilde{\varepsilon}$ would need to be increased by a factor of $\sqrt{6}$, from 5×10^{-5} a.u. to 1.225×10^{-4} a.u.

Fig. 8a plots the corresponding polariton spectrum at normal incidence (yellow line). This spectrum contains four polariton peaks, which is very different from the case of a single-mode cavity, i.e., when only the lowest-frequency cavity mode ($l_x = 1$) is included in the simulation (red line). Moreover, in the ω_{\parallel} -dependent polariton spectrum (Fig. 8b), cavity #3 exhibits an even more complicated polariton spectrum than Fig. 7b, thus strongly indicating significant interaction between cavity photons at different ω_{\parallel} .

3. Cavity #4

Lastly, consider an extreme example — cavity #4. Here, all molecular grid points are accumulated at the middle of the cavity mirror plane (along the x -direction), while all the other parameters remain the same as cavity #1. This cavity setup could be regarded as a naive generalization of the single-mode Pauli–Fierz Hamiltonian to the multi-mode case. For this cavity, the corresponding polariton spectrum, as illustrated in Fig. 9, becomes very complicated. As shown in Fig. 9a, many peaks coexist in the polariton spectrum at normal incidence (yellow line). Moreover, in the ω_{\parallel} -dependent polariton spectrum (Fig. 9b), any well-defined polariton branch or avoided crossing completely disappears. Hence, cavity #4 fails completely to mimic the polariton dispersion relation in VSC experiments. This failure emphasizes the fact that the long-wave approximation (i.e., approximating the whole molecular system as localized at a single point) fails when including many ω_{\parallel} -dependent cavity modes.

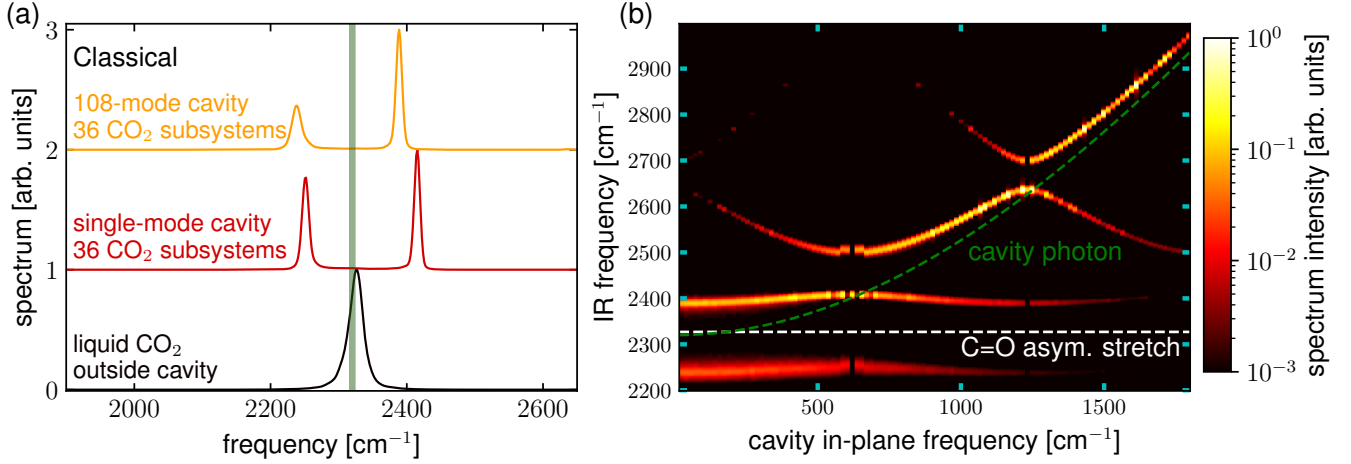


FIG. 7. Similar plots as Figs. 5a,b except that cavity #1 is replaced by cavity #2; i.e., 108 (instead of 36) cavity modes are used during the simulation.

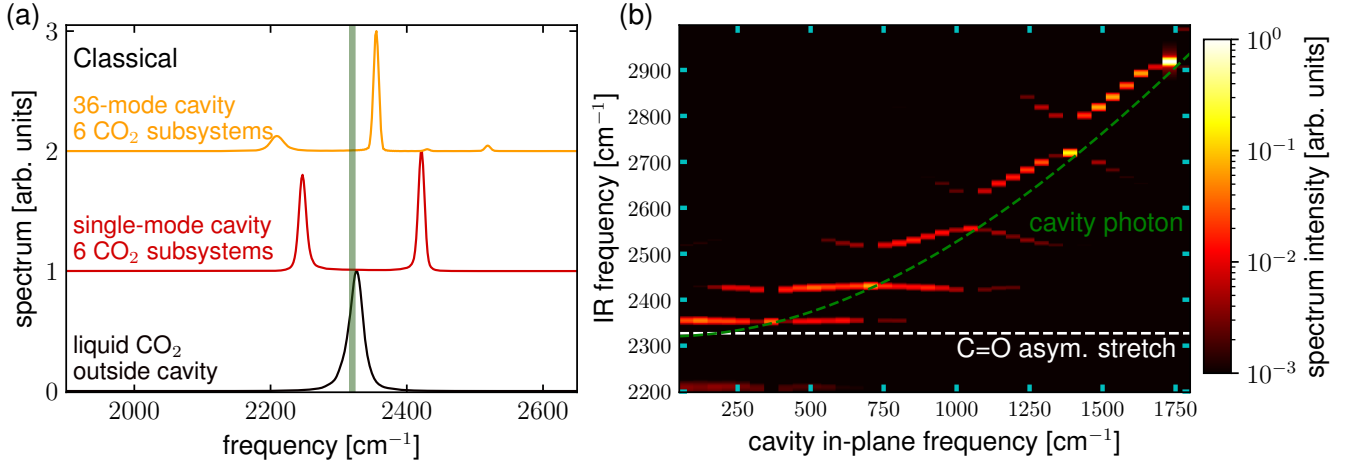


FIG. 8. Similar plots as Figs. 5a,b except that here cavity #1 is replaced by cavity #3; i.e., only $N_{\text{grid}} = 6$ (instead of $N_{\text{grid}} = 36$) grid points are used during the simulation and the molecular distribution along the cavity mirror plane (the x -direction) becomes very sparse.

C. Cavity #5: a 2D cavity setup

After demonstrating the results for several 1D cavities, we found that only the parameter set for cavity #1 can be used to represent Fabry-Pérot cavities. However, given that most VSC experiments thus far have employed 2D Fabry-Pérot cavities, it is critical to further evaluate the capabilities of our code by directly simulating 2D cavities. After all, the photonic density of states for 1D cavities differs significantly from that for 2D cavities.

As shown in Fig. 4 and Table I, cavity #5 extends the parameter set of cavity #1 to 2D, i.e., with a 2D molecular grid of size 36×36 (1296 grid points). For such a 2D cavity setup, the cavity frequencies can take

$$\omega_c(l_x, l_y) = \sqrt{\omega_{\perp}^2 + l_x^2 \Delta\omega_x^2 + l_y^2 \Delta\omega_y^2}, \quad (39)$$

where $\omega_{\perp} = 2320 \text{ cm}^{-1}$, $\Delta\omega_{x,y} = 50 \text{ cm}^{-1}$, and $l_{x,y} = 1, 2, \dots, 18$.

Fig. 10 plots the polariton dispersion relation of cavity #5 after an equilibrium CavMD simulation. We fix $\omega_y \equiv l_y \Delta\omega_y$ and plot $\omega_x \equiv l_x \Delta\omega_x$ for several values of ω_y : (a) 50 cm^{-1} , (b) 550 cm^{-1} , and (c) 900 cm^{-1} . As ω_y is increased, the three slices of the polariton dispersion relation show the transition from on-resonance strong coupling at $\omega_x \approx 0$ to complete off-resonance. Clearly, cavity #5 can be regarded as a 2D model of realistic planar Fabry-Pérot cavities.

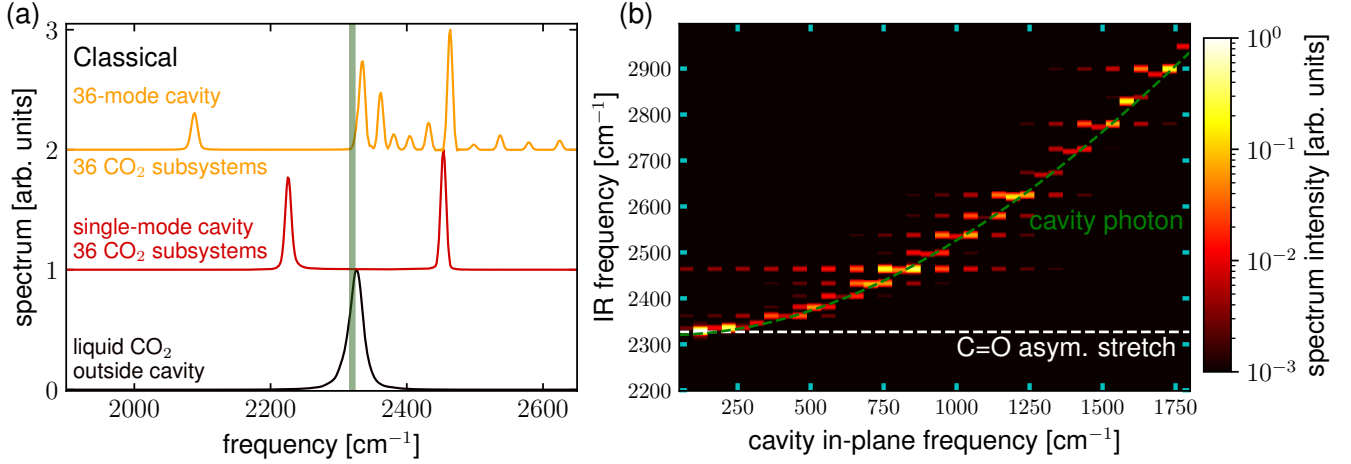


FIG. 9. Similar plots as Figs. 5a,b except that here cavity #1 is replaced by cavity #4; i.e., the spatial variance of different molecular grid points is eliminated and the long wave approximation is taken.

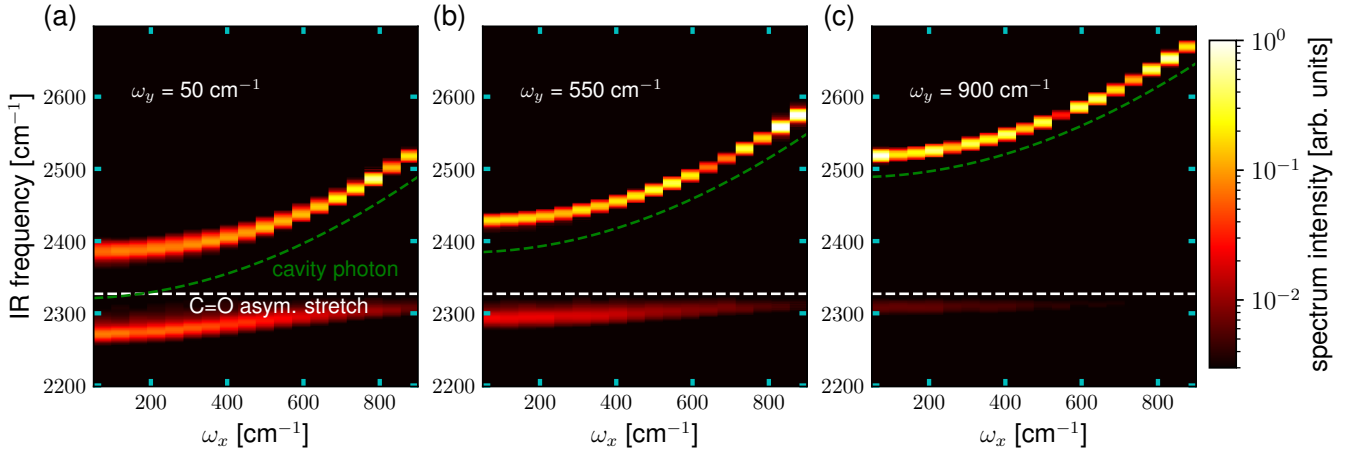


FIG. 10. The polariton dispersion relations for cavity #5 (a 2D cavity) as a function of $\omega_x \equiv l_x \Delta \omega_x$, the in-plane frequency along the x -direction, when $\omega_y \equiv l_y \Delta \omega_y$ is chosen as (a) 50 cm^{-1} , (b) 550 cm^{-1} , and (c) 900 cm^{-1} .

V. DISCUSSION

After performing simulations on cavity #1-#5, we have learned that obtaining a numerical solution to VSC in planar Fabry-Pérot cavities is nontrivial. On the one hand, the computational cost must be bearable in the simulation of Fabry-Pérot VSC. To this end, both the cavity modes at different ω_{\parallel} and the molecular distribution need to be discretized. On the other hand, an inappropriate discretization scheme may break the single-mode approximation and produce inconsistent results when compared with experiments. Hence, one must wonder which discretization scheme is valid.

A. The role of in-plane translational symmetry in planar Fabry-Pérot cavities

Before discussing how to prepare an appropriate discretization scheme, let us briefly review the reason why the single-mode approximation is valid to describe the linear-response polariton spectrum in planar Fabry-Pérot cavities. As discussed by Agranovich et al., the polariton eigenvalues in a planar Fabry-Pérot cavity can be obtained by solving the eigenequation below:⁶⁷

$$\alpha(\mathbf{k}_{\parallel})[\omega - \omega_c(k_{\parallel})] = \sum_i T_i^*(\mathbf{k}_{\parallel}) \sum_{\mathbf{k}'_{\parallel}} T_i(\mathbf{k}'_{\parallel}) \alpha(\mathbf{k}'_{\parallel}) / [\omega - \omega_0]. \quad (40)$$

Here, $|\alpha(\mathbf{k}_{\parallel})|^2$ denotes the photonic weight of the polaritons at \mathbf{k}_{\parallel} ; ω_0 denotes the molecular excitation frequency; $T_i(\mathbf{k}_{\parallel})$ denotes the light-matter coupling between the cavity photon mode at \mathbf{k}_{\parallel} and the i -th molecule. Al-

though the explicit form of $T_i(\mathbf{k}_{\parallel})$ can be multivariate,⁶⁷ we are interested only in its dependence on the in-plane phase of the cavity modes. To this end, we can write

$$T_i(\mathbf{k}_{\parallel}) = T_i e^{i\mathbf{k}_{\parallel} \cdot \mathbf{r}_{\parallel}^{(i)}}, \quad (41)$$

where T_i denotes the prefactor, and $\mathbf{r}_{\parallel}^{(i)}$ denotes the molecular position along the cavity mirror plane. Assuming T_i as a constant and $\alpha(\mathbf{k}_{\parallel}) \approx \alpha(\mathbf{k}'_{\parallel})$, we can rewrite Eq. (40) as

$$[\omega - \omega_c(k_{\parallel})][\omega - \omega_0] \approx \sum_i \sum_{\mathbf{k}'_{\parallel}} |T_i|^2 e^{-i(\mathbf{k}_{\parallel} - \mathbf{k}'_{\parallel}) \cdot \mathbf{r}_{\parallel}^{(i)}}. \quad (42)$$

Given a homogeneous distribution of molecules along the cavity mirror plane, the summation in Eq. (42) over $\mathbf{k}'_{\parallel} \neq \mathbf{k}_{\parallel}$ should cancel out with each other. Mathematically speaking, the translational symmetry along the cavity mirror plane gives $\sum_i e^{-i(\mathbf{k}_{\parallel} - \mathbf{k}'_{\parallel}) \cdot \mathbf{r}_{\parallel}^{(i)}} \propto \int d\mathbf{r}_{\parallel} e^{-i(\mathbf{k}_{\parallel} - \mathbf{k}'_{\parallel}) \cdot \mathbf{r}_{\parallel}} \propto \delta(\mathbf{k}_{\parallel} - \mathbf{k}'_{\parallel})$, i.e., the summation \sum_i can be replaced by a simple integral $\int d\mathbf{r}_{\parallel}$ only when the molecular distribution is homogeneous along the cavity mirror plane. When $\sum_i e^{-i(\mathbf{k}_{\parallel} - \mathbf{k}'_{\parallel}) \cdot \mathbf{r}_{\parallel}^{(i)}}$ is replaced by $\delta(\mathbf{k}_{\parallel} - \mathbf{k}'_{\parallel})$, Eq. (42) becomes

$$[\omega - \omega_c(k_{\parallel})][\omega - \omega_0] = \text{const.} \quad (43)$$

Eq. (43) is the polariton eigenequation under the single-mode approximation, i.e., the cavity modes at different k_{\parallel} effectively do not interact with each other. Note that to derive Eq. (43) from Eq. (42), we must apply the in-plane translational symmetry.

B. How to satisfy in-plane translational symmetry numerically?

As shown above, the (continuous) in-plane translational symmetry is the key to obtain the polariton eigenequation under the single-mode approximation. In our simulations, both the cavity modes at different ω_{\parallel} and the molecular distribution are discretized, so the continuous in-plane translational symmetry is of course no longer preserved.

However, the loss of continuous in-plane translational symmetry does not preclude numerical simulation of planar Fabry–Pérot cavities. Instead, we believe that preserving discrete in-plane translational symmetry is adequate. For our 1D Fabry–Pérot-like cavity setups, analogous to the cancellation of the $\mathbf{k}'_{\parallel} \neq \mathbf{k}_{\parallel}$ terms in Eq. (42), it is necessary to reduce the following error function

$$\text{Err}(k_x) = \frac{1}{N_{\text{grid}}} \sum_{i=1}^{N_{\text{grid}}} \sum_{k'_x \neq k_x} \sin(k'_x x_i) \sin(k_x x_i) \rightarrow 0 \quad (44)$$

TABLE II. Statistics of $\text{Err}(k_x)$ [Eq. (44)] for the 1D cavity setups. Here, the percentage of $\text{Err}(k_x) \neq 0$ is defined as the percentage of $\text{Err}(k_x)$ satisfying $|\text{Err}(k_x)| > 10^{-3}$.

cavity	$\langle \text{Err}(k_x) \rangle$	percentage of $\text{Err}(k_x) \neq 0$
#1	0.00	0%
#2	0.34	35%
#3	0.42	44%
#4	0.50	50%

to zero for any given k_x , where x_i denotes the location of the i -th grid point.

Given the parameters of the cavity setups in Table I, in Table II we provide the statistics of the error function $\text{Err}(k_x)$ for each 1D cavity setup. While, for cavity #1, $\text{Err}(k_x)$ is always exactly equal to zero for arbitrary k_x , for cavities #2, #3, and #4, a finite percentage of $\text{Err}(k_x)$ has been found to be non-zero for various k_x values. Because we have learned that only cavity #1 can be used to represent Fabry–Pérot cavities employed in experiments, Eq. (44) appears to be a good criterion to check whether the discrete translational symmetry is satisfied for the numerical setups of 1D cavities. Moreover, Table II appears to indicate that both the absolute average $\langle |\text{Err}(k_x)| \rangle$ and the percentage of $\text{Err}(k_x) \neq 0$ may have a positive correlation with the breakdown of the single-mode approximation: the larger these values, the less the polariton dispersion relation is consistent with experimental findings.

In summary, to numerically simulate 1D Fabry–Pérot cavities, which we can use to interpret experiments, we need to guarantee Eq. (44). Of course, it is also necessary to have a sufficient number of photon modes as well as molecular grid points. Although our discussion above focused on 1D cavities, the conclusion can also be generalized to 2D cavities. It appears that to numerically preserve the translational symmetry of 2D cavities (e.g., cavity #5), one just needs to make sure the cavity parameters for each dimension preserve the discrete translational symmetry [Eq. (44)] independently.

C. Do cavities in the absence of in-plane translational symmetry have physical meaning?

With the above discussion in mind, one may treat cavity #2–#4 as a few (unphysical) counterexamples of how to break the in-plane translational symmetry. However, we also want to emphasize that cavity #2–#4 could have real physical meaning. In experiments, if one could prepare cavities with two sets of parallel cavity mirrors along both the z - and x -directions and then distribute molecules (probably in the solid state) in a similar manner as in cavity #2–#4 (see Fig. 4), one might be able to observe the complicated polariton spectra in Figs. 7–9. These complicated polariton spectra might provide a flexible approach for controlling polariton-polariton scattering and may find wide applications in the future.

Even for 2D Fabry–Pérot cavities used in experiments, by nonuniformly distributing molecules along the cavity mirror plane, one could also observe very complicated polariton dispersion relations. A more comprehensive investigation in this direction is reported elsewhere.⁶⁸

D. Approaching the macroscopic limit

Finally, we demonstrate how to approach the macroscopic limit in the framework of mesoscale CavMD. To simplify our discussion, we will focus on cavity #1, which corresponds to a 1D cavity. In order to determine whether the simulation results of cavity #1 can be used to understand experiments in the macroscopic limit, we will increase the system size and repeat the simulations in Sec. IV.

Table III provides six sets of cavity parameters for our simulations, denoted by cavity #1.X.Y. Here, for each cavity setup, as compared with cavity #1, the N_{grid} is increased by a factor of X and the cavity mode number (N_{mode}) is increased by a factor of Y . When these two parameters are increased, $\tilde{\varepsilon} \propto 1/\sqrt{N_{\text{grid}}}$ is reduced proportionally to maintain the fixed Rabi splitting. The frequency spacing between the neighboring cavity modes, $\Delta\omega_x = 50.0 \text{ cm}^{-1}/Y$, is also reduced such that the maximal frequency of the simulated cavity modes remains unchanged. When $X = Y$, this enlarging process has a physical meaning of increasing the cavity length along the x -direction by a factor of $X = Y$ while fixing the molecular density distribution along the cavity mirror plane. When $X \neq Y$, the molecular density distribution along the cavity mirror plane is no longer fixed. All the other simulation details are the same as those in Sec. III.

Fig. 11 plots the simulated polariton dispersion relations for the six enlarged cavities listed in Table III. As shown in Figs. 11a-c, the polariton dispersion relations remain the same when both N_{grid} and N_{mode} are increased proportionally ($X = Y = 4, 16, 64$). More interestingly, Fig. 11d shows that the consistent polariton dispersion relation can also be obtained by increasing only N_{grid} , leaving N_{mode} unchanged ($X = 4, Y = 1$). However, Figs. 11e,f suggest that setting $Y > X$ leads to polariton dispersion relations breaking the single-mode approximation.

As discussed previously, numerically preserving the in-plane translational symmetry [or satisfying Eq. (44)] is crucial for validating the single-mode approximation. Because this symmetry should also be preserved as the system size is increased, Eq. (44) in general limits the possible combinations of N_{mode} and N_{grid} . The examples of cavity #1-#5 and #1.X.Y appear to suggest that given a fixed N_{grid} , ensuring $N_{\text{mode}} \lesssim N_{\text{grid}}$ can yield reasonable polariton dispersion relations. Although it is unclear whether the upper bound of $N_{\text{mode}} \lesssim N_{\text{grid}}$ should hold for a general set of 1D parameters, one might understand this upper bound for our parameters as follows: When $N_{\text{mode}} > N_{\text{grid}}$, it becomes impossible to assign every cav-

ity mode to interact with an independent molecular state (as represented by a linearly independent combination of grid points, or $\sqrt{1/N_{\text{grid}}} \sum_i s_i \mathbf{b}_i \sin(k_x x_i)$, where s_i denotes the coefficient and \mathbf{b}_i represents the basis for a single grid point); at least one such a molecular state would have to interact directly with multiple cavity modes, thus violating the single-mode approximation.

The polariton-polariton scattering dynamics in Fig. 12 provide additional insights when increasing the system size. If N_{grid} and N_{mode} are increased proportionally, as shown in Fig. 12a, the polariton-polariton scattering dynamics remain largely unchanged. However, Fig. 12b demonstrates that polariton-polariton scattering can be greatly suppressed if only N_{grid} is increased and N_{mode} remains the same as in cavity #1 (cavity #1.4.1), despite this cavity setup giving reasonable polariton dispersion relations (Fig. 11d). Such a suppressed behavior can be understood as follows. The excited polaritons at $\omega_c = 2396 \text{ cm}^{-1}$ can transfer energy to two possible channels: the molecular dark modes with zero photonic contribution, and the polaritons at different in-plane frequencies. When only the N_{grid} is increased, the number of molecular dark modes is increased; because N_{mode} remains unchanged, the number of polaritons in the system remains the same. As a result, when only N_{grid} is increased, the excited polaritons at $\omega_c = 2396 \text{ cm}^{-1}$ would be more likely to transfer energy to the dark modes and the polariton-polariton scattering would be greatly suppressed. Overall, one necessary condition to numerically obtain the non-negligible polariton-polariton scattering events in the macroscopic limit is to increase N_{grid} (or more precisely, the number of simulated molecules, N_{simu}) and N_{mode} proportionally when enlarging the system size.

VI. CONCLUSION

To summarize, we have provided a mesoscale CavMD formalism for studying VSC with Fabry–Pérot-like cavities. The examples of cavities #1-#5 showcase the importance of preserving the in-plane translational symmetry for capturing the ω_{\parallel} -dependent polariton dispersion relation observed in experiments. Additionally, our nonequilibrium CavMD simulations have provided initial evidence of elastic vibrational polariton-polariton scattering at nearest neighbor ω_{\parallel} . We have also demonstrated the protocol to approach the macroscopic limit, i.e., by enlarging the system size while reducing the light-matter coupling per molecule (or maintaining the constant Rabi splitting).

Our code may serve as an advantageous simulation approach when either the molecular detail (such as the dark modes or chemical reactions) or photonic structure plays crucial roles in the processes of interest. For example, CavMD could be used as a numerical tool to investigate vibrational polariton transport⁴² and explore the experimental conditions necessary to prepare vibrational po-

TABLE III. Parameters for cavity setups of different system sizes. The notation cavity #1.X.Y means that, as compared to cavity #1 in Table I, N_{grid} is increased by a factor of X and the cavity mode number ($N_{\text{mode}} = l_x^{\text{max}}$) is increased by a factor of Y .

cavity	ω_{\perp} [cm $^{-1}$]	$\Delta\omega_x$ [cm $^{-1}$]	$\Delta\omega_y$ [cm $^{-1}$]	l_x^{max}	l_y^{max}	N_{grid}	x grid positions [L_x]	y grid positions [L_y]	$\tilde{\epsilon}$ [a.u.]
#1.4.4	2320	12.5	0	144	1	144	$[6.9 \times 10^{-3}, 1.38 \times 10^{-2}, \dots, 0.9931]$	[0.0]	2.5×10^{-5}
#1.16.16	2320	3.125	0	576	1	576	$[1.7 \times 10^{-3}, 3.47 \times 10^{-3}, \dots, 0.9983]$	[0.0]	1.25×10^{-5}
#1.64.64	2320	0.781	0	2304	1	2304	$[4.34 \times 10^{-4}, 8.68 \times 10^{-4}, \dots, 0.9996]$	[0.0]	6.25×10^{-6}
#1.4.1	2320	50.0	0	36	1	144	$[6.9 \times 10^{-3}, 1.38 \times 10^{-2}, \dots, 0.9931]$	[0.0]	2.5×10^{-5}
#1.4.6	2320	8.33	0	216	1	144	$[6.9 \times 10^{-3}, 1.38 \times 10^{-2}, \dots, 0.9931]$	[0.0]	2.5×10^{-5}
#1.4.8	2320	6.25	0	288	1	144	$[6.9 \times 10^{-3}, 1.38 \times 10^{-2}, \dots, 0.9931]$	[0.0]	2.5×10^{-5}

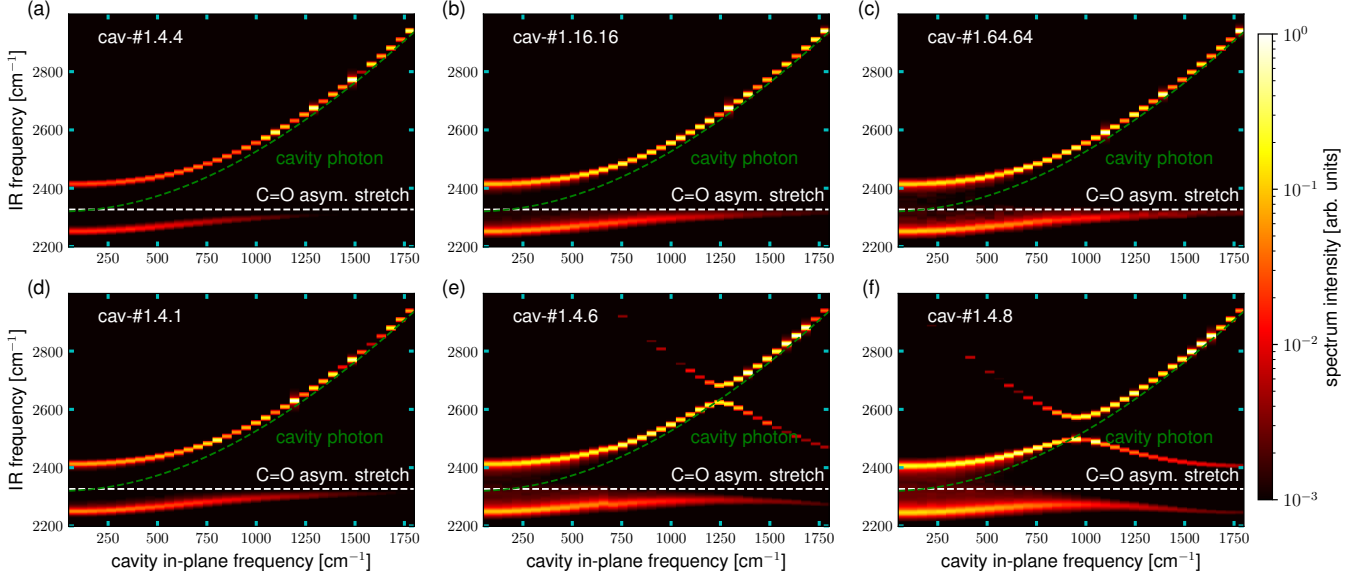


FIG. 11. Simulated polariton dispersion relations corresponding to the six cavity setups in Table III. For cavity #1.64.64 (part c), only 10 equilibrium trajectories were simulated to obtain the spectrum, while for each of the other cavity setups, 40 equilibrium trajectories were simulated.

lariton condensates,⁶⁹ theoretical hypotheses that have not been experimentally observed. In addition, with a QM/MM description of the molecules,⁵⁰ this code can be used to numerically examine various hypotheses on the origin of the VSC catalytic effects observed in the Ebbesen experiments.

Moreover, as the formalism of mesoscale CavMD is derived from a general Power–Zienau–Woolley Hamiltonian, our CavMD scheme is gauge invariant and can be easily extended to more complicated photonic environments.^{9,70–75} For instance, by switching the photonic mode functions of a rectangular parallelepiped [Eq. (23)] to those of a plasmonic nanostructure, plus a QM or QM/MM description of the molecules, one can use this code to study plasmonic catalysis under both weak and strong couplings. Overall, many exciting research opportunities are enabled by mesoscale CavMD. Of course, if one is interested in only linear polariton spectroscopy, it becomes cumbersome to perform expensive molecular dynamics simulations instead of using simplified approaches.^{33,45,76}

In the end, we emphasize that the simulation results

for cavities #2–#4 also highlight a research opportunity under VSC. Specifically, if the molecular distribution along the cavity mirror plane does not preserve the in-plane translational symmetry, more complicated k_{\parallel} -dependent polariton dispersion relations could be experimentally observed. Such a possible avenue is worthy of further investigation, as it provides more flexibility to tune polariton-polariton interactions at different k_{\parallel} values than conventional homogeneous Fabry–Pérot cavities.

APPENDIX: INCLUDING CAVITY LOSS

The cavity loss has been turned off throughout the calculations above. As a side note, here we briefly discuss the effects of cavity loss on our simulations. Overall, including cavity loss is very straightforward within the framework of CavMD⁵⁵ — the photonic equation of motion in Eq. (28b) needed to be replaced by the following form:

$$m_{k\lambda} \ddot{q}_{k\lambda} = -m_{k\lambda} \omega_k^2 \tilde{q}_{k\lambda} - \tilde{\epsilon}_{k\lambda} q_{g,k\lambda}^{\text{sub}} - \gamma_{k\lambda} \dot{\tilde{p}}_{k\lambda} + \eta_{k\lambda}(t), \quad (45)$$

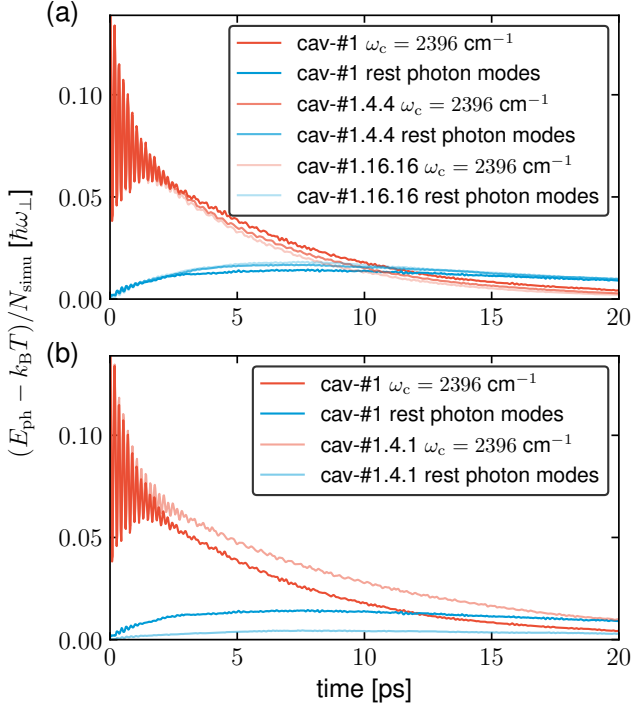


FIG. 12. Polariton-polariton scattering dynamics corresponding to a few cavity setups in Table III. The polariton-polariton scattering dynamics for cavity #1 (plotted in Fig. 6a) are included in both parts for comparison. For cavities with different system sizes, the cavity mode at the same frequency $\omega_c = 2396 \text{ cm}^{-1}$ is initially excited; the initial photon energy is increased proportionally to N_{grid} so that the excitation per molecule $[(E_{\text{ph}} - k_B T)/N_{\text{simu}}]$, the y -axis] remains the same.

where $\gamma_{k\lambda}$ and $\eta_{k\lambda}(t)$ denote the damping rate and the Langevin white noise for each cavity mode, respectively. In other words, a standard Langevin thermostat is attached on top of each cavity mode.

Fig. 13a plots the polariton spectrum at normal incidence corresponding to the cavity #1 in Fig. 5a when the cavity lifetime is set as $1/\gamma_{k\lambda} \equiv 300 \text{ fs}$ (yellow line). Here, the polariton linewidth is broadened as compared to the case of the lossless cavity (red line). The polariton dispersion relation in Fig. 13b also obviously demonstrates the polariton linewidth broadening in the lossy cavity. Note that when the simulation trajectories were used to calculate the polariton spectra in the lossy cavity, only the cavity modes (not molecules) were coupled to the Langevin thermostat.

VII. ACKNOWLEDGMENTS

This material is based upon the work supported by the start-up funds from the University of Delaware Department of Physics and Astronomy. This research is supported in part through the use of Information Technologies (IT) resources at the University of Delaware,

specifically the high-performance computing resources. This work also uses computing resources supported by the AWS Cloud Credit for Research program.

VIII. DATE AVAILABILITY STATEMENT

The code and input files are available on Github at <https://github.com/TaoELi/cavity-md-ipi>.

- ¹A. Shalabney, J. George, J. Hutchison, G. Pupillo, C. Genet, and T. W. Ebbesen, “Coherent Coupling of Molecular Resonators with a Microcavity Mode,” *Nat. Commun.* **6**, 5981 (2015).
- ²J. P. Long and B. S. Simpkins, “Coherent Coupling between a Molecular Vibration and Fabry–Perot Optical Cavity to Give Hybridized States in the Strong Coupling Limit,” *ACS Photonics* **2**, 130–136 (2015).
- ³A. Thomas, J. George, A. Shalabney, M. Dryzhakov, S. J. Varma, J. Moran, T. Chervy, X. Zhong, E. Devaux, C. Genet, J. A. Hutchison, and T. W. Ebbesen, “Ground-State Chemical Reactivity under Vibrational Coupling to the Vacuum Electromagnetic Field,” *Angew. Chemie Int. Ed.* **55**, 11462–11466 (2016).
- ⁴A. D. Dunkelberger, B. T. Spann, K. P. Fears, B. S. Simpkins, and J. C. Owrutsky, “Modified Relaxation Dynamics and Coherent Energy Exchange in Coupled Vibration-Cavity Polaritons,” *Nat. Commun.* **7**, 1–10 (2016).
- ⁵A. Thomas, L. Lethuillier-Karl, K. Nagarajan, R. M. A. Vergauwe, J. George, T. Chervy, A. Shalabney, E. Devaux, C. Genet, J. Moran, and T. W. Ebbesen, “Tilting a Ground-State Reactivity Landscape by Vibrational Strong Coupling,” *Science* **363**, 615–619 (2019).
- ⁶B. Xiang, R. F. Ribeiro, M. Du, L. Chen, Z. Yang, J. Wang, J. Yuen-Zhou, and W. Xiong, “Intermolecular Vibrational Energy Transfer Enabled by Microcavity Strong Light–Matter Coupling,” *Science* **368**, 665–667 (2020).
- ⁷T.-T. Chen, M. Du, Z. Yang, J. Yuen-Zhou, and W. Xiong, “Cavity-enabled Enhancement of Ultrafast Intramolecular Vibrational Redistribution over Pseudorotation,” *Science* **378**, 790–794 (2022).
- ⁸W. Ahn, J. F. Triana, F. Recabal, F. Herrera, and B. S. Simpkins, “Modification of Ground-State Chemical Reactivity via Light–Matter Coherence in Infrared Cavities,” *Science* **380**, 1165–1168 (2023).
- ⁹A. D. Wright, J. C. Nelson, and M. L. Weichman, “Rovibrational Polaritons in Gas-Phase Methane,” *J. Am. Chem. Soc.* **145**, 5982–5987 (2023).
- ¹⁰R. F. Ribeiro, L. A. Martínez-Martínez, M. Du, J. Campos-Gonzalez-Angulo, and J. Yuen-Zhou, “Polariton Chemistry: Controlling Molecular Dynamics with Optical Cavities,” *Chem. Sci.* **9**, 6325–6339 (2018).
- ¹¹T. E. Li, B. Cui, J. E. Subotnik, and A. Nitzan, “Molecular Polaritons: Chemical Dynamics Under Strong Light–Matter Coupling,” *Annu. Rev. Phys. Chem.* **73**, 43–71 (2022).
- ¹²J. Fregoni, F. J. Garcia-Vidal, and J. Feist, “Theoretical Challenges in Polaritonic Chemistry,” *ACS Photonics* **9**, 1096–1107 (2022).
- ¹³B. S. Simpkins, A. D. Dunkelberger, and I. Vurgaftman, “Control, Modulation, and Analytical Descriptions of Vibrational Strong Coupling,” *Chem. Rev.* **123**, 5020–5048 (2023).
- ¹⁴A. Mandal, M. A. Taylor, B. M. Weight, E. R. Koessler, X. Li, and P. Huo, “Theoretical Advances in Polariton Chemistry and Molecular Cavity Quantum Electrodynamics,” *Chem. Rev.* **123**, 9786–9879 (2023).
- ¹⁵M. Ruggenthaler, D. Sidler, and A. Rubio, “Understanding Polaritonic Chemistry from Ab Initio Quantum Electrodynamics,” *Chem. Rev.* **123**, 11191–11229 (2023), arXiv:2211.04241.
- ¹⁶M. V. Imperatore, J. B. Asbury, and N. C. Giebink, “Reproducibility of Cavity-Enhanced Chemical Reaction Rates in the

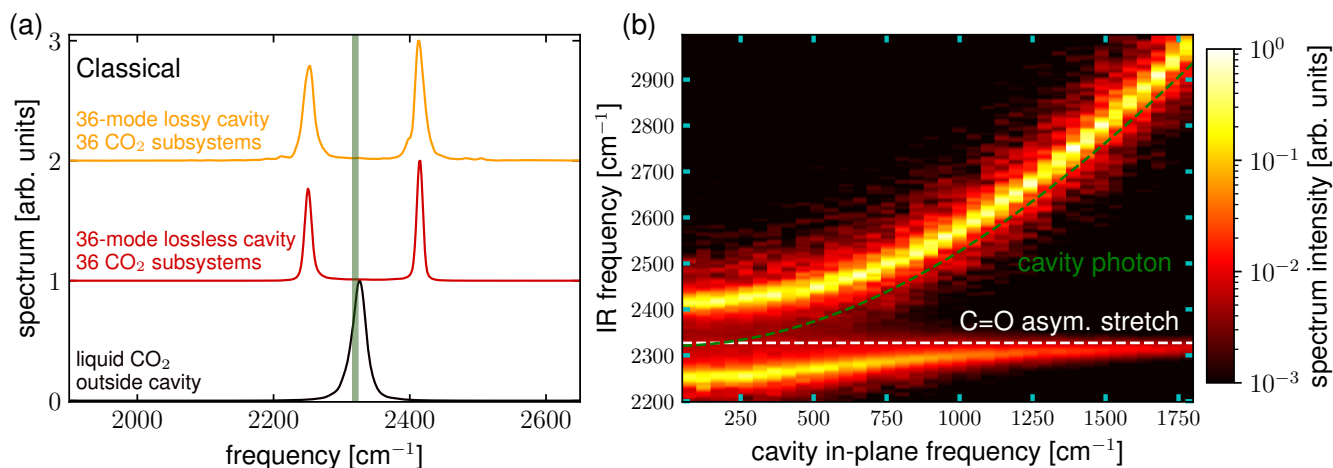


FIG. 13. Polariton spectra from classical CavMD simulations. (a) The normalized IR spectrum of liquid CO₂ outside the cavity (black), coupled to a 36-mode lossless cavity (red, Fig. 5a), or a 36-mode lossy cavity with the cavity lifetime as $1/\gamma_{k\lambda} \equiv 300$ fs (yellow). (b) The polariton spectrum vs the cavity in-plane frequency ω_{\parallel} corresponding to the lossy 36-mode cavity. The simulation conditions inside the 36-mode cavity are identical to those in Figs. 5a,b (cavity #1).

- Vibrational Strong Coupling Regime,” *J. Chem. Phys.* **154**, 191103 (2021).
- ¹⁷G. D. Wiesehan and W. Xiong, “Negligible Rate Enhancement from Reported Cooperative Vibrational Strong Coupling Catalysis,” *J. Chem. Phys.* **155**, 241103 (2021).
- ¹⁸A. P. Fidler, L. Chen, A. M. McKillop, and M. L. Weichman, “Ultrafast Dynamics of CN Radical Reactions with Chloroform Solvent under Vibrational Strong Coupling,” *J. Chem. Phys.* **159**, 164302 (2023), arXiv:2307.04875.
- ¹⁹J. Galego, C. Climent, F. J. Garcia-Vidal, and J. Feist, “Cavity Casimir-Polder Forces and Their Effects in Ground-State Chemical Reactivity,” *Phys. Rev. X* **9**, 021057 (2019).
- ²⁰J. A. Campos-Gonzalez-Angulo, R. F. Ribeiro, and J. Yuen-Zhou, “Resonant Catalysis of Thermally Activated Chemical Reactions with Vibrational Polaritons,” *Nat. Commun.* **10**, 4685 (2019).
- ²¹N. M. Hoffmann, L. Lacombe, A. Rubio, and N. T. Maitra, “Effect of Many Modes on Self-Polarization and Photochemical Suppression in Cavities,” *J. Chem. Phys.* **153**, 104103 (2020).
- ²²X. Li, A. Mandal, and P. Huo, “Cavity Frequency-Dependent Theory for Vibrational Polariton Chemistry,” *Nat. Commun.* **12**, 1315 (2021).
- ²³E. W. Fischer and P. Saalfrank, “Ground State Properties and Infrared Spectra of Anharmonic Vibrational Polaritons of Small Molecules in Cavities,” *J. Chem. Phys.* **154**, 104311 (2021).
- ²⁴P. Y. Yang and J. Cao, “Quantum Effects in Chemical Reactions under Polaritonic Vibrational Strong Coupling,” *J. Phys. Chem. Lett.* **12**, 9531–9538 (2021).
- ²⁵D. S. Wang, T. Neuman, S. F. Yelin, and J. Flick, “Cavity-Modified Unimolecular Dissociation Reactions via Intramolecular Vibrational Energy Redistribution,” *J. Phys. Chem. Lett.* **13**, 3317–3324 (2022).
- ²⁶J. Flick, M. Ruggenthaler, H. Appel, and A. Rubio, “Atoms and Molecules in Cavities, from Weak to Strong Coupling in Quantum-Electrodynamics (QED) Chemistry,” *Proc. Natl. Acad. Sci.* **114**, 3026–3034 (2017).
- ²⁷R. R. Riso, T. S. Haugland, E. Ronca, and H. Koch, “Molecular Orbital Theory in Cavity QED Environments,” *Nat. Commun.* **13**, 1368 (2022).
- ²⁸C. Schäfer, J. Flick, E. Ronca, P. Narang, and A. Rubio, “Shining Light on the Microscopic Resonant Mechanism Responsible for Cavity-Mediated Chemical Reactivity,” *Nat. Commun.* **13**, 7817 (2022).
- ²⁹J. Bonini and J. Flick, “Ab Initio Linear-Response Approach to Vibro-polaritons in the Cavity Born-Oppenheimer Approximation,” *J. Chem. Theory Comput.* **18**, 2764–2773 (2021).
- ³⁰J. Yang, Q. Ou, Z. Pei, H. Wang, B. Weng, Z. Shuai, K. Mullen, and Y. Shao, “Quantum-Electrodynamical Time-Dependent Density Functional Theory within Gaussian Atomic Basis,” *J. Chem. Phys.* **155**, 064107 (2021).
- ³¹B. Rosenzweig, N. M. Hoffmann, L. Lacombe, and N. T. Maitra, “Analysis of the Classical Trajectory Treatment of Photon Dynamics for Polaritonic Phenomena,” *J. Chem. Phys.* **156**, 054101 (2022).
- ³²J. F. Triana, F. J. Hernández, and F. Herrera, “The Shape of the Electric Dipole Function Determines the Sub-picosecond Dynamics of Anharmonic Vibrational Polaritons,” *J. Chem. Phys.* **152**, 234111 (2020).
- ³³T. E. Li, J. E. Subotnik, and A. Nitzan, “Cavity Molecular Dynamics Simulations of Liquid Water under Vibrational Ultrastrong Coupling,” *Proc. Natl. Acad. Sci.* **117**, 18324–18331 (2020).
- ³⁴T. S. Haugland, E. Ronca, E. F. Kjønstad, A. Rubio, and H. Koch, “Coupled Cluster Theory for Molecular Polaritons: Changing Ground and Excited States,” *Phys. Rev. X* **10**, 041043 (2020).
- ³⁵J. P. Philbin, T. S. Haugland, T. K. Ghosh, E. Ronca, M. Chen, P. Narang, and H. Koch, “Molecular van der Waals Fluids in Cavity Quantum Electrodynamics,” *J. Phys. Chem. Lett.* **14**, 8988–8993 (2023), arXiv:2209.07956.
- ³⁶H. Deng, H. Haug, and Y. Yamamoto, “Exciton-Polariton Bose-Einstein Condensation,” *Rev. Mod. Phys.* **82**, 1489–1537 (2010).
- ³⁷J. Keeling and S. Kéna-Cohen, “Bose-Einstein Condensation of Exciton-Polaritons in Organic Microcavities,” *Annu. Rev. Phys. Chem.* **71**, 435–459 (2020).
- ³⁸H. L. Luk, J. Feist, J. J. Toppari, and G. Groenhof, “Multiscale Molecular Dynamics Simulations of Polaritonic Chemistry,” *J. Chem. Theory Comput.* **13**, 4324–4335 (2017).
- ³⁹R. H. Tichauer, J. Feist, and G. Groenhof, “Multi-scale Dynamics Simulations of Molecular Polaritons: The Effect of Multiple Cavity Modes on Polariton Relaxation,” *J. Chem. Phys.* **154**, 104112 (2021).
- ⁴⁰I. Sokolovskii, R. H. Tichauer, D. Morozov, J. Feist, and G. Groenhof, “Multi-scale Molecular Dynamics Simulations of Enhanced Energy Transfer in Organic Molecules under Strong Coupling,” *Nature Communications* **14**, 6613 (2023),

- arXiv:2209.07309.
- ⁴¹M. Sukharev, J. Subotnik, and A. Nitzan, “Dissociation Slowdown by Collective Optical Response under Strong Coupling Conditions,” *J. Chem. Phys.* **158**, 084104 (2023).
- ⁴²E. Suyabatmaz and R. F. Ribeiro, “Vibrational Polariton Transport in Disordered Media,” *J. Chem. Phys.* **159**, 034701 (2023), arXiv:2303.05474.
- ⁴³W. Ying, M. A. D. Taylor, and P. Huo, “Resonance Theory of Vibrational Polariton Chemistry at the Normal Incidence,” *Nanophotonics*, <https://doi.org/10.1515/nanoph-2023-0685> (2024).
- ⁴⁴T. E. Li, A. Nitzan, S. Hammes-Schiffer, and J. E. Subotnik, “Quantum Simulations of Vibrational Strong Coupling via Path Integrals,” *J. Phys. Chem. Lett.* **13**, 3890–3895 (2022).
- ⁴⁵A. Z. Lieberherr, S. T. Furniss, J. E. Lawrence, and D. E. Manolopoulos, “Vibrational Strong Coupling in Liquid Water from Cavity Molecular Dynamics,” *J. Chem. Phys.* **158**, 234106 (2023).
- ⁴⁶T. E. Li, A. Nitzan, and J. E. Subotnik, “Polariton Relaxation under Vibrational Strong Coupling: Comparing Cavity Molecular Dynamics Simulations against Fermi’s Golden Rule Rate,” *J. Chem. Phys.* **156**, 134106 (2022).
- ⁴⁷T. E. Li, A. Nitzan, and J. E. Subotnik, “Cavity Molecular Dynamics Simulations of Vibrational Polariton-enhanced Molecular Nonlinear Absorption,” *J. Chem. Phys.* **154**, 094124 (2021).
- ⁴⁸B. Xiang and W. Xiong, “Molecular Vibrational Polariton: Its Dynamics and Potentials in Novel Chemistry and Quantum Technology,” *J. Chem. Phys.* **155**, 050901 (2021).
- ⁴⁹T. E. Li, A. Nitzan, and J. E. Subotnik, “Energy-Efficient Pathway for Selectively Exciting Solute Molecules to High Vibrational States via Solvent Vibration-Polariton Pumping,” *Nat. Commun.* **13**, 4203 (2022).
- ⁵⁰T. E. Li and S. Hammes-Schiffer, “QM/MM Modeling of Vibrational Polariton Induced Energy Transfer and Chemical Dynamics,” *J. Am. Chem. Soc.* **145**, 377–384 (2023).
- ⁵¹C. Cohen-Tannoudji, J. Dupont-Roc, and G. Grynberg, *Photons and Atoms: Introduction to Quantum Electrodynamics* (Wiley, New York, 1997) pp. 280–295.
- ⁵²To derive Eq. (11) from Eq. (3), we have used the following identities: $-\frac{1}{\epsilon_0} \int d\mathbf{r} \mathbf{D}_\perp(\mathbf{r}) \cdot \hat{\mathcal{P}}_\perp(\mathbf{r}) = -\frac{1}{\epsilon_0} \int d\mathbf{r} \mathbf{D}_\perp(\mathbf{r}) \cdot \hat{\mathcal{P}}(\mathbf{r})$, and $\frac{1}{2\epsilon_0} \int d\mathbf{r} |\hat{\mathcal{P}}_\perp(\mathbf{r})|^2 = \frac{1}{2\epsilon_0} \int d\mathbf{r} \int d\mathbf{r}' \hat{\mathcal{P}}(\mathbf{r}) \hat{\delta}_\perp(\mathbf{r} - \mathbf{r}') \hat{\mathcal{P}}(\mathbf{r}')$.
- ⁵³J. Flick, H. Appel, M. Ruggenthaler, and A. Rubio, “Cavity Born–Oppenheimer Approximation for Correlated Electron–Nuclear–Photon Systems,” *J. Chem. Theory Comput.* **13**, 1616–1625 (2017).
- ⁵⁴W. P. Schleich, *Quantum Optics in Phase Space* (Wiley, 2001) p. 232.
- ⁵⁵T. E. Li, A. Nitzan, and J. E. Subotnik, “Collective Vibrational Strong Coupling Effects on Molecular Vibrational Relaxation and Energy Transfer: Numerical Insights via Cavity Molecular Dynamics Simulations,” *Angew. Chemie Int. Ed.* **60**, 15533–15540 (2021).
- ⁵⁶J. Horak, D. Sidler, W.-M. Huang, M. Ruggenthaler, and A. Rubio, “Analytic Model for Molecules Under Collective Vibrational Strong Coupling in Optical Cavities,” , arXiv:2401.16374. arXiv.org ePrint archive. <http://arxiv.org/abs/2401.16374> (accessed Jan 29, 2024) (2024), arXiv:2401.16374.
- ⁵⁷T. Schnappinger, D. Sidler, M. Ruggenthaler, A. Rubio, and M. Kowalewski, “Cavity Born–Oppenheimer Hartree–Fock Ansatz: Light–Matter Properties of Strongly Coupled Molecular Ensembles,” *J. Phys. Chem. Lett.* **14**, 8024–8033 (2023), arXiv:2307.02208.
- ⁵⁸D. Sidler, T. Schnappinger, A. Obzhairov, M. Ruggenthaler, M. Kowalewski, and A. Rubio, “Unraveling a Cavity-Induced Molecular Polarization Mechanism from Collective Vibrational Strong Coupling,” *J. Phys. Chem. Lett.* **15**, 5208–5214 (2024).
- ⁵⁹T. E. Markland and M. Ceriotti, “Nuclear Quantum Effects Enter the Mainstream,” *Nat. Rev. Chem.* **2**, 0109 (2018).
- ⁶⁰V. Kapil, M. Rossi, O. Marsalek, R. Petraglia, Y. Litman, T. Spura, B. Cheng, A. Cuzzocrea, R. H. Meißner, D. M. Wilkins, B. A. Helfrecht, P. Juda, S. P. Bienvenue, W. Fang, J. Kessler, I. Poltavsky, S. Vandenbrande, J. Wieme, C. Corminboeuf, T. D. Kühne, D. E. Manolopoulos, T. E. Markland, J. O. Richardson, A. Tkatchenko, G. A. Tribello, V. Van Speybroeck, and M. Ceriotti, “I-PI 2.0: A Universal Force Engine for Advanced Molecular Simulations,” *Comput. Phys. Commun.* **236**, 214–223 (2019).
- ⁶¹M. Rossi, M. Ceriotti, and D. E. Manolopoulos, “How to Remove the Spurious Resonances from Ring Polymer Molecular Dynamics,” *J. Chem. Phys.* **140**, 234116 (2014).
- ⁶²D. A. McQuarrie, *Statistical Mechanics* (Harper-Collins Publishers, New York, 1976).
- ⁶³M.-P. Gaigeot and M. Sprik, “Ab Initio Molecular Dynamics Computation of the Infrared Spectrum of Aqueous Uracil,” *J. Phys. Chem. B* **107**, 10344–10358 (2003).
- ⁶⁴S. Habershon, G. S. Fanourgakis, and D. E. Manolopoulos, “Comparison of Path Integral Molecular Dynamics Methods for the Infrared Absorption Spectrum of Liquid Water,” *J. Chem. Phys.* **129**, 074501 (2008).
- ⁶⁵A. Nitzan, *Chemical Dynamics in Condensed Phases: Relaxation, Transfer and Reactions in Condensed Molecular Systems* (Oxford University Press, New York, 2006).
- ⁶⁶M. Rossi, V. Kapil, and M. Ceriotti, “Fine Tuning Classical and Quantum Molecular Dynamics Using a Generalized Langevin Equation,” *J. Chem. Phys.* **148**, 102301 (2018), arXiv:1704.05099.
- ⁶⁷V. M. Agranovich, M. Litinskaia, and D. G. Lidzey, “Cavity Polaritons in Microcavities Containing Disordered Organic Semiconductors,” *Phys. Rev. B* **67**, 085311 (2003).
- ⁶⁸T. E. Li, “Vibrational Polaritons with Broken In-Plane Translational Symmetry,” , arXiv:2403.12411. arXiv.org ePrint archive. <http://arxiv.org/abs/2403.12411> (accessed Mar 19, 2024) (2024), arXiv:2403.12411.
- ⁶⁹S. Pannir-Sivajothi, J. A. Campos-Gonzalez-Angulo, L. A. Martínez-Martínez, S. Sinha, and J. Yuen-Zhou, “Driving chemical reactions with polariton condensates,” *Nat. Commun.* **13**, 1645 (2022).
- ⁷⁰J. Gautier, M. Li, T. W. Ebbesen, and C. Genet, “Planar Chirality and Optical Spin–Orbit Coupling for Chiral Fabry–Perot Cavities,” *ACS Photonics* **9**, 778–783 (2022), arXiv:2105.08605.
- ⁷¹K. Voronin, A. S. Taradin, M. V. Gorkunov, and D. G. Baranov, “Single-Handedness Chiral Optical Cavities,” *ACS Photonics* **9**, 2652–2659 (2022), arXiv:2104.14230.
- ⁷²R. R. Riso, L. Grazioli, E. Ronca, T. Giovannini, and H. Koch, “Strong Coupling in Chiral Cavities: Nonperturbative Framework for Enantiomer Discrimination,” *Phys. Rev. X* **13**, 031002 (2023), arXiv:2209.01987.
- ⁷³C. Schäfer and D. G. Baranov, “Chiral Polaritonics: Analytical Solutions, Intuition, and Use,” *J. Phys. Chem. Lett.* **14**, 3777–3784 (2023), arXiv:2209.07177.
- ⁷⁴A. Canales, O. V. Kotov, B. Küçüköz, and T. O. Shegai, “Self-Hybridized Vibrational-Mie Polaritons in Water Droplets,” *Phys. Rev. Lett.* **132**, 193804 (2024).
- ⁷⁵D. Yoo, F. de León-Pérez, M. Pelton, I.-H. Lee, D. A. Mohr, M. B. Raschke, J. D. Caldwell, L. Martín-Moreno, and S.-H. Oh, “Ultrastrong Plasmon–Phonon Coupling via Epsilon-Near-Zero Nanocavities,” *Nat. Photonics* **15**, 125–130 (2021), arXiv:2003.00136.
- ⁷⁶Y. Zhu, D. J. Gauthier, S. E. Morin, Q. Wu, H. J. Carmichael, and T. W. Mossberg, “Vacuum Rabi Splitting as a Feature of Linear-Dispersion Theory: Analysis and Experimental Observations,” *Phys. Rev. Lett.* **64**, 2499–2502 (1990).